



**THE EFFECTS OF MULTI-STATIC
PROCESSING AND AUTOFOCUSING ON
AN EXPERIMENTAL PASSIVE SYNTHETIC
APERTURE RADAR IMAGING SYSTEM**

THESIS

Nicolas H. Zimmerman, Capt, USAF
AFIT-ENG-MS-17-M-085

**DEPARTMENT OF THE AIR FORCE
AIR UNIVERSITY**

AIR FORCE INSTITUTE OF TECHNOLOGY

Wright-Patterson Air Force Base, Ohio

DISTRIBUTION STATEMENT A
APPROVED FOR PUBLIC RELEASE; DISTRIBUTION UNLIMITED.

The views expressed in this document are those of the author and do not reflect the official policy or position of the United States Air Force, the United States Department of Defense or the United States Government. This material is declared a work of the U.S. Government and is not subject to copyright protection in the United States.

AFIT-ENG-MS-17-M-085

THE EFFECTS OF MULTI-STATIC PROCESSING AND AUTOFOCUSING ON
AN EXPERIMENTAL PASSIVE SYNTHETIC APERTURE RADAR IMAGING
SYSTEM

THESIS

Presented to the Faculty
Department of Electrical and Computer Engineering
Graduate School of Engineering and Management
Air Force Institute of Technology
Air University
Air Education and Training Command
in Partial Fulfillment of the Requirements for the
Degree of Master of Science in Electrical Engineering

Nicolas H. Zimmerman, B.S.A.E.

Capt, USAF

March 2017

DISTRIBUTION STATEMENT A
APPROVED FOR PUBLIC RELEASE; DISTRIBUTION UNLIMITED.

AFIT-ENG-MS-17-M-085

THE EFFECTS OF MULTI-STATIC PROCESSING AND AUTOFOCUSING ON
AN EXPERIMENTAL PASSIVE SYNTHETIC APERTURE RADAR IMAGING
SYSTEM

THESIS

Nicolas H. Zimmerman, B.S.A.E.
Capt, USAF

Committee Membership:

Dr. Julie A. Jackson
Chair

Dr. Peter J. Collins
Member

Lt Col Phillip M. Corbell, PhD
Member

Abstract

The Air Force Institute of Technology (AFIT) Radar Instrumentation Lab (RAIL) Synthetic Aperture Radar (SAR) experimental system is capable of bistatic passive SAR collections. This research assesses current system limitations and expands the hardware and software to facilitate multi-static imaging in experimental and simulated configurations. An autofocus algorithm is applied to phase history data to mitigate the effects of position error and improve image quality in both bistatic and multi-static cases. Final experimental results show significant qualitative improvement to imaging products attributed to these signal processing techniques.

Acknowledgements

The following thesis does not represent the work of an individual. I owe its completion to many influential people. Dr. Julie Jackson was the primary source of direction, education, and technical advice. Her deep theoretical knowledge and relentless patience extracted the best from me. My colleagues in the LORE group were always there to commiserate and answer my imponderable questions.

But this is really for my wife. She is my best friend, the ultimate companion, and the very essence of loveliness. But Darling, next time I have a thesis due in February, lets not get pregnant in November...

Nicolas H. Zimmerman

Table of Contents

	Page
Abstract	iv
Acknowledgements	v
List of Figures	viii
List of Tables	x
I. Introduction	1
1.1 Introduction to Multi-Static Passive SAR	1
1.2 Importance of Passive SAR	2
1.3 The AFIT SAR System	3
1.4 Key Assumptions	4
1.5 Methodology	6
1.6 Scope of Research Effort	6
1.7 Relevance of Research	7
II. In the Laboratory	9
2.1 Introduction	9
2.2 Lab Setup	9
2.2.1 Laboratory Background	9
2.2.2 Laboratory Modifications	14
2.3 Laboratory Design Tradeoffs	17
2.3.1 Sampling Rate Study	17
2.3.2 Waveforms	18
2.4 Laboratory Design Challenges	19
2.4.1 Scene Geometry	19
2.4.2 Wave Curvature Analysis	21
2.4.3 Data Generation and Analysis	22
2.4.4 Calibration	22
2.5 Methodology	25
2.5.1 Data Collection	25
2.5.2 Image Processing	27
2.5.3 Multistatic Imaging through Coherent Summation	28
2.5.4 Extended Aperture Image Processing	29
2.5.5 Resolution	30
2.6 Error Sources	33

	Page
III. Autofocusing Enhancements	39
3.1 Introduction	39
3.2 Background	39
3.3 Mathematical Modeling of Calibration and Position Error	39
3.4 Results from Simulation	43
3.4.1 Case I: No induced error	44
3.4.2 Case II: Rotational error	44
3.4.3 Case III: White noise error	46
3.5 Autofocus Applied to Experimental Results	47
3.5.1 Example Results from Experimentation	47
3.5.2 Robustness of Autofocusing Algorithm	48
3.6 Conclusion	52
IV. Final Imaging Results	53
4.1 Dynamic range challenges	53
4.2 Resolution Analysis	54
4.3 Effects of Pulse Dropping on Image Quality	57
4.4 Extended Aperture Processing Comparison	57
V. Conclusions and Future Work	62
5.1 Summary	62
5.2 Future work	62
Bibliography	65

List of Figures

Figure		Page
1	SAR imaging techniques	2
2	System photographs	4
3	Matlab GUI main menu	12
4	Waveform generation interface	13
5	Oscilloscope Fastframe(TM) visualization	13
6	RAIL laboratory configuration	15
7	Radar targets	17
8	Scene configuration in laboratory	20
9	Bistatic scene geometry	21
10	Range profiles	24
11	Comparison of SAR imaging techniques	25
12	Antenna pattern overlaid on scene	26
13	Sampled pulse example	27
14	SAR image overlaid onto laboratory environment	28
15	Multistatic image coherent summation	29
16	Comparison of SAR multistatic synthesis techniques	30
17	SAR resolution	31
18	Effects of position error	35
19	Stationary antenna effects on image quality	36
20	Background subtraction	38
21	Example of unfocused SAR image	38
22	Spotlight mode SAR	40

Figure	Page
23	Differential range 41
24	Case I: Focusing with no error 44
25	Case II: Focusing skew error 45
26	Case III: Focusing white noise error 47
27	Autofocused image example 48
28	Autofocused outdoor scene 49
29	Effects of position error on autofocus 49
30	Autofocusing away from target 50
31	Effects of position error on autofocus 51
32	Focusing without target present 52
33	Dynamic range effects 54
34	Downrange resolution performance 55
35	Crossrange resolution performance 56
36	Unfocused pulse dropping 58
37	Focused pulse dropping 59
38	Extended aperture processing 60
39	Extended aperture processing resolution 61

List of Tables

Table		Page
1	Calculated Scene Resolution	33
2	Case I Peak Target Reflections	44
3	Case II Peak Target Reflections	45
4	Case III Peak Target Reflections	46

THE EFFECTS OF MULTI-STATIC PROCESSING AND AUTOFOCUSING ON AN EXPERIMENTAL PASSIVE SYNTHETIC APERTURE RADAR IMAGING SYSTEM

I. Introduction

The proliferation of modern consumer electronic devices is overcrowding the radio frequency (RF) spectrum. With no relief in sight, future systems must minimize their RF footprint to operate effectively, which has spurred a growing interest in passive sensing techniques. Passive systems do not transmit at all, but leverage selected signals already present in the environment to accomplish their mission. This research effort investigates the application of passive techniques to synthetic aperture radar (SAR) imaging in the context of the Radar Instrumentation Laboratory (RAIL) at the Air Force Institute of Technology (AFIT). This thesis builds upon previous AFIT RAIL setups for bistatic SAR [1–3] and develops a laboratory system and procedure for multi-static, passive SAR imaging experiments. An autofocusing algorithm is applied to the results to enhance laboratory image quality. Data gathered by such a system is useful for algorithm development and future system evolution.

1.1 Introduction to Multi-Static Passive SAR

An active SAR radar system illuminates a target with many pulses of RF energy and processes the returns from the target into a two-dimensional image. SAR remote sensing technology has many applications including ground mapping from an aircraft or spacecraft, imaging an aircraft or spacecraft from the ground, monitoring oceanic activity, medical imaging, geographic surveillance, navigation, and astronomy [4].

This research effort is directed at airborne ground mapping applications, though its results may be used broadly.

SAR imaging has many advantages over optical or infrared imaging. RF can travel through inclement weather with little attenuation compared to wavelengths in the visible or infrared spectrum and is not degraded in nighttime conditions. SAR maintains fine resolution independent of the system's range, unlike optical imaging systems. The negative aspects of SAR imaging include equipment complexity and required processing power [5].

A passive SAR system produces similar images to an active system but uses signals already present in the environment. In a bistatic passive system, a single receiver can be designed to exploit signals from a geographically separated transmitting source. Multi-static systems employ any number of separate transmitters and receivers to create an image of the desired scene as shown in Figure 1.

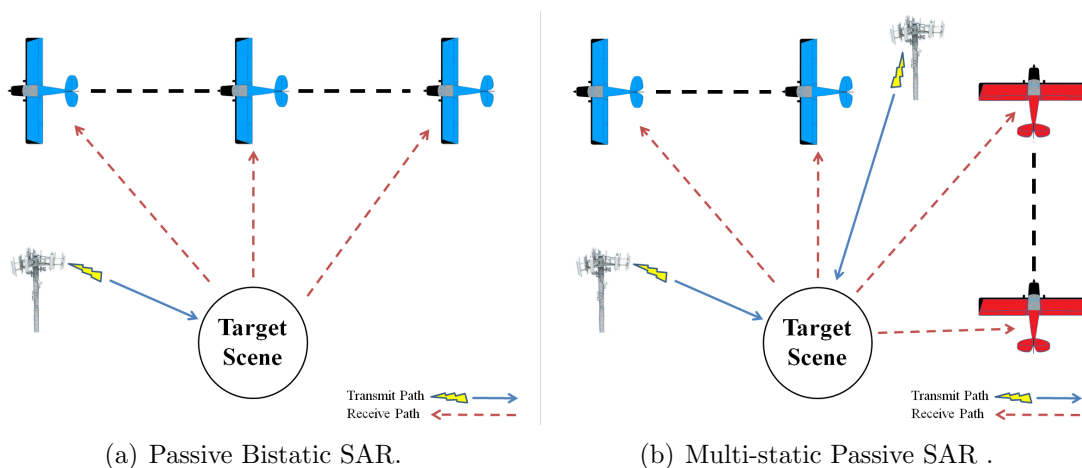


Figure 1. Bistatic and multistatic SAR imaging techniques

1.2 Importance of Passive SAR

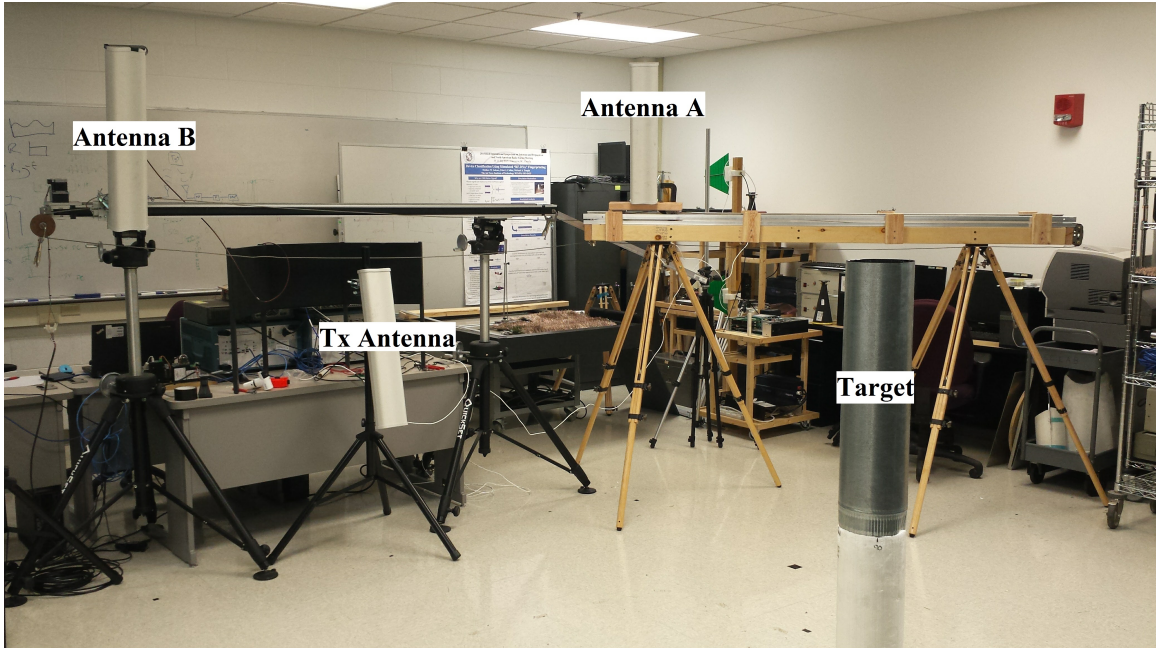
Modern RF systems must compete for frequency allocation in the congested RF spectrum. Active transmissions require authorized bandwidth, which is increasingly

rare and, in contested environments, are susceptible to interception, exploitation, reverse targeting, and jamming. Military missions often require radio silence, which excludes the use of a SAR transmitter.

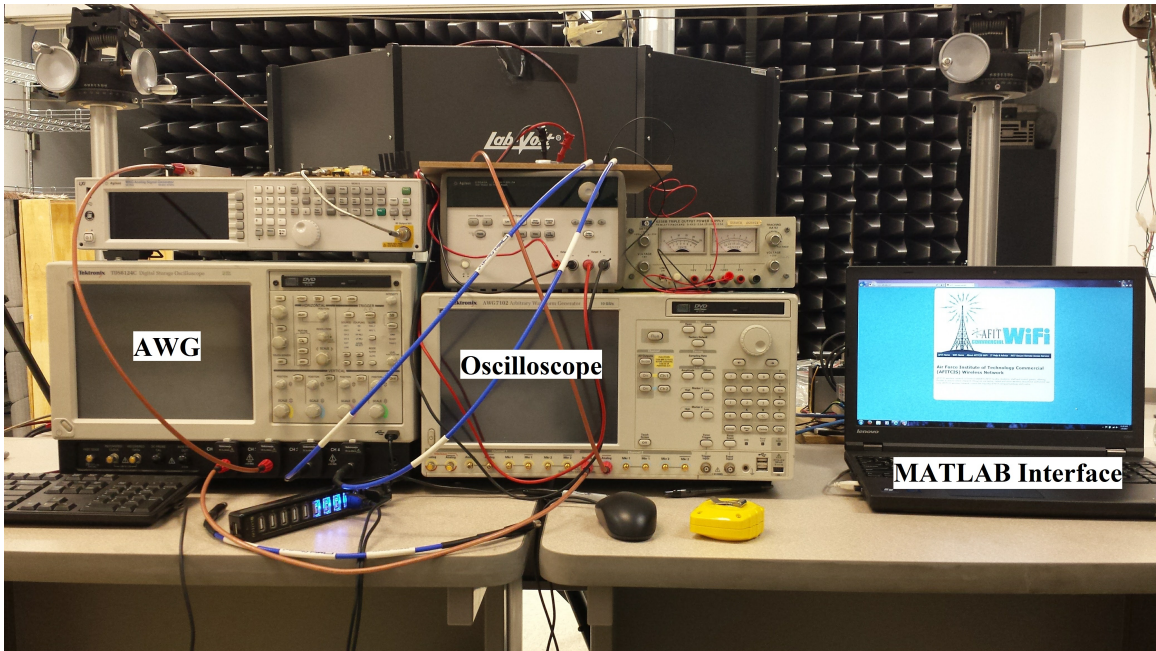
1.3 The AFIT SAR System

Prior research in this area has been conducted at AFIT [1–3] using a rudimentary SAR system developed for use in AFIT’s RAIL (Figure 2). All of these research efforts have investigated the feasibility of using orthogonal frequency division multiplexing (OFDM) signals in a passive SAR system. Gutierrez del Arroyo [2] created a prototype passive SAR system using Worldwide Interoperability for Microwave Access (WiMAX) signals to create a scene image with multiple targets. The receive antenna was manually moved between collections and kept still while receiving [2] which is referenced as a “move-stop-move” collection in this thesis. Schmidt extended the capabilities of the system to enable moving data collections where the receive antenna is in constant motion during the collection sequence. Regardless of the collection methodology, SAR image quality largely depends on accurate position solutions for both transmit and receive antennae. Images produced by Schmidt in small laboratory spaces suffered from antenna position error and target positions were not directly discernible. This paper refers to these raw images as “unfocused.”

The logical next step is to investigate multi-static collection capabilities, find and analyze sources of error in the system, and employ calibration techniques to mitigate errors. The Schmidt experiments can then be re-accomplished to validate improvements. The resulting data are manipulated with an autofocusing algorithm developed by Aaron Evers [6] to further mitigate errors and produce focused imagery.



(a) Antenna rails and transmit antenna.



(b) Data collection and control console.

Figure 2. The AFIT RAIL SAR System

1.4 Key Assumptions

Like any physical system, RF waves are affected by myriad phenomena while traveling in the atmosphere and interacting with an image scene. These complexities

prevent modern imaging systems from processing radar returns into perfect images. Some assumptions are necessary to adequately simplify the data collection and processing methods for laboratory measurement.

- All features in the scene are assumed to be stationary. This assumption is especially valid indoors, as air movement will have a very negligible affect on the targets. The stationary scene assumption eliminates the need for Doppler processing. It has been shown that the RAIL's moving receiver antenna is not capable of moving fast enough to cause a noticeable Doppler shift [1].
- The test apparatus simulates a SAR scene requiring a stripmap algorithm, but all data processing is accomplished using spotlight signal processing. Previous AFIT research [1] assumed that alternative processing techniques had a negligible affect on the data, but the validity of this assumption will be discussed more thoroughly in Chapter II.
- Multi-static image generation is accomplished by coherently summing the results across each bistatic pair.
- The receive antenna is assumed to be stationary when transmitting and receiving a pulse. This assumption is valid when the speed of light is far greater than the speed of the moving antenna, which is true in this lab scenario as the receive antenna moves $17 \mu\text{m}$ from the beginning of transmission to the last sampling of a given pulse by the oscilloscope.
- For accurate image generation, the exact location of the transmit and receive antenna must be known. The current lab apparatus does not communicate this information, and it must be estimated. The sensitivity of results to position error will be investigated more thoroughly in Chapter II.

1.5 Methodology

All system development and measurements for this research effort took place in AFIT's RAIL laboratory with major components from the previous AFIT systems incorporated into the multi-static setup. The transmit path consists of a laptop computer, which generates a waveform through a Matlab interface. This waveform is passed to the Tektronix arbitrary waveform generator (AWG) 7102 and through a Micro Circuits amplifier before radiating from an AirMax sector antenna, as shown in Figure 2.

The receive path begins with an AirMax sector antenna followed by a Micro Circuits low noise amplifier and uses a Tektronix TDS6124 Oscilloscope sampling at 10 Gs/s. The oscilloscope is capable of sampling up to three receiver chains allowing for multi-static expansion. The data are manually passed to the laptop, which uses another Matlab interface to synthesize an image. Many target types and scene geometries are analyzed to deduce the effect of radar cross section (RCS), distance, and angular separation on system performance.

1.6 Scope of Research Effort

The goal of this research effort is to deliver a functioning multi-static, passive SAR system and produce high-quality laboratory SAR images of a basic scene. Chapter II outlines the current state-of-the-art in passive SAR with special emphasis on work performed in AFIT's RAIL, which details the selection of the OFDM waveform and subsequent development of the system. Applicable theory is also explored.

Chapter II also discusses the new system developments and configuration. Lab safety is addressed, as the design of experiments is explained. Preliminary multi-static results are presented for comparison with results from the legacy system. Possible sources of error in the system are outlined as are mitigation strategies. Chapter III

presents the results obtained from multi-static experimentation with and without an autofocus algorithm applied. Chapter IV summarizes these research findings and provides a vector for future research efforts.

This thesis makes these specific contributions to the multistatic passive radar community and AFIT research efforts:

- Updates AFIT RAIL passive bistatic imaging system to allow for multistatic collections and data processing.
- Transforms system calibration process from a “guess and test” technique to a simple automated algorithm.
- Investigates error sources and applies autofocusing algorithm to significantly enhance the quality of laboratory images.
- Analyzes limitations of current AFIT RAIL passive multistatic imaging system.

1.7 Relevance of Research

Research results are used to determine the feasibility of an airborne or vehicle-borne passive SAR system using OFDM signals. Completion of this research effort establishes a strong baseline for scaling up to a practical passive SAR laboratory system for future data collection and algorithm testing for algorithms developed at AFIT, Air Force Research Laboratory (AFRL), and other institutions. Future algorithms will enable passive sensing capabilities superior to those of current systems. Areas of particular relevance will be discussed throughout this thesis.

This research effort is highly applicable to many current research efforts and military technologies. In subsequent efforts, the RAIL system will be continually developed and refined to achieve levels of performance unprecedented for inexpensive

laboratory systems. Data will be distributed to interested communities to foster more research efforts.

II. In the Laboratory

2.1 Introduction

This research builds upon the efforts of other AFIT students in the iterative design and development of AFIT's current SAR system. Whereas previous AFIT research has concentrated mostly on the suitability of common communication signals for the purposes of SAR, this study uses a single signal with known characteristics to develop a multi-static passive SAR system to produce high-quality laboratory SAR images of a basic scene.

While much has been published on passive systems and multi-static systems, these combined characteristics form a newer research area that has appeal in both military and scientific applications. The discussion is predicated on a fundamental knowledge of radar principles and signal processing.

2.2 Lab Setup

Passive multi-static radar systems typically operate with multiple radar receivers employing one or more transmitters. Transmitted signals may be known to receiver operators but most likely they are non-cooperative, or not controlled by the radar engineer. This research employs a stationary, pseudo-cooperative transmitter (the transmitted signal is given to the post processing software) and multiple receivers on mobile platforms.

2.2.1 Laboratory Background.

Significant developmental effort has been applied to AFIT's SAR in past years to develop the current system. Mr. Aaron Evers and Maj Jose Gutierrez developed a Matlab *passive radar toolbox*, which performed move-stop-move data collections

using an AWG, oscilloscope, and antenna apparatus. [3, 7–9]. Their system’s data collection time was measured in hours for a single collection due to software and memory limitations. Nevertheless, it functioned well and produced useful results.

Flt Lt Dayne Schmidt attempted to characterize the system’s sources of error and expand its capability to enable moving receiver data collections and Doppler shift processing [1]. Schmidt overcame previous hardware limitations by enabling a new oscilloscope mode that significantly reduced memory requirements. Previously, the oscilloscope continued sampling each pulse long after the pulse ceased transmitting. Using the TekTronics TDS6124 FastFrameTM feature, oscilloscope sampling is triggered by the waveform transmission from the arbitrary waveform generator, and sampling continues for a short, predetermined time period, ultimately reducing memory requirements. A complete description of the laboratory configuration at the outset of this research effort is available in previous theses [1, 3].

Moving data collections produced data with more errors than move-stop-move collections had previously, and Schmidt hypothesized that motion measurement error (MME) and Doppler frequency shifts were responsible for the loss of fidelity in his results [1]. Schmidt carefully constructed a simulation of the AFIT system and environment and generated data with and without a Doppler shift for comparison purposes. He ultimately concluded that Doppler shift was not a significant source of error, and the MMEs were primarily to blame. Schmidt’s updates to the system reduced data collection time from hours to seconds. Though moving collections will be used in this analysis, Doppler compensation is not accounted for in the passive radar toolbox.

2.2.1.1 Laptop and the Matlab Interface.

The laptop is a Dell Latitude D630 using Matlab version 2011. The computer is networked to the AWG and oscilloscope using TekVISA Resource Manager version 3.3.4.6 and communicates with the antenna rail motor using Oriental Motor Company's Immediate Motion Creator software version 2.02.

The main menu of the graphical user interface (GUI) is shown in Figure 3. From this menu, the user may generate a waveform or select the type of collection to perform. Not all functions on this menu are supported by more recent changes to the GUI code. The data collection algorithm primarily used in this research is accessed by the "MOVING COLLECTION" option on the main menu. From the "MOVING COLLECTION" GUI, the user is able to set the parameters of the data collection, select the transmit waveform, control the motorized linear track, and run the collection scenario. The GUI has built-in error checks to ensure the parameters are realistic, Nyquist criteria is met, and the collection will not overburden the oscilloscope.

2.2.1.2 Waveforms and the Arbitrary Waveform Generator.

If "GENERATE WAVEFORM" is selected from the main menu, a window appears to prompt the user for details regarding the desired waveform (Figure 4). This feature allows the user to customize waveform parameters specific to the desired application. The waveform, once generated, is passed to the AWG, where it awaits transmission.

The transmitter is a Tektronix AWG 7102 capable of sampling at 10 GS/s. Two channel outputs allow transmission of two separate signals to create a multi-static environment, and a trigger output communicates the exact timing of the pulse transmission to the oscilloscope. The oscilloscope uses this input to trigger sampling only, it does not record or manipulate this data further. The waveform generated in the Matlab interface is used for all post-processing purposes. Thus, the system is not pas-

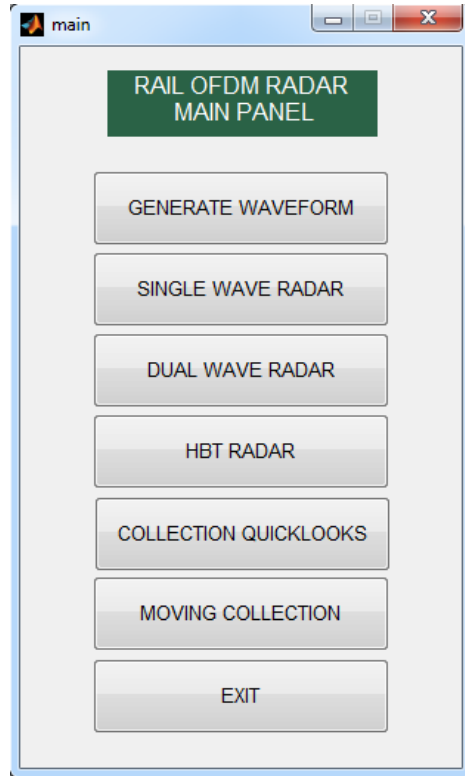


Figure 3. Matlab GUI main menu

sive in the strictest sense but utilizes many processing schemes and data manipulation techniques required in passive radar processing.

2.2.1.3 Oscilloscope.

The Tektronix TDS6124 Oscilloscope has four channel inputs with a selectable sample rate. Based on the transmit frequency of 2.5 GHz, the minimum available sample rate of 10 GS/s is used. Memory capacity of this device is 32 mega-samples per channel allowing for 0.0064 seconds of sampling. This limitation necessitated activation of the system's FastFrame™ feature. In FastFrame™ mode, oscilloscope sampling is activated through reception of a trigger pulse from the output of the AWG and continues for a user-defined interval. After this interval, sampling ceases and the oscilloscope waits for another trigger to continue sampling, as shown in Figure 5.

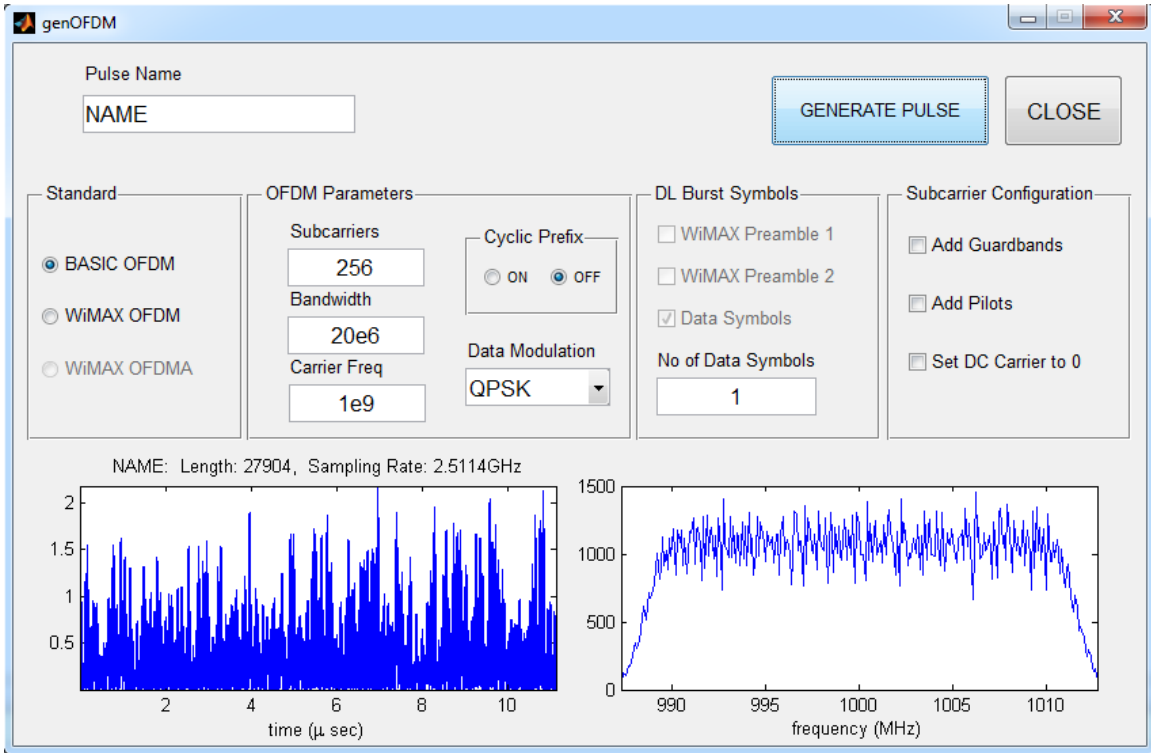


Figure 4. Waveform generation interface

The FastFrameTM mode allows for many pulses to be sampled, while ignoring the

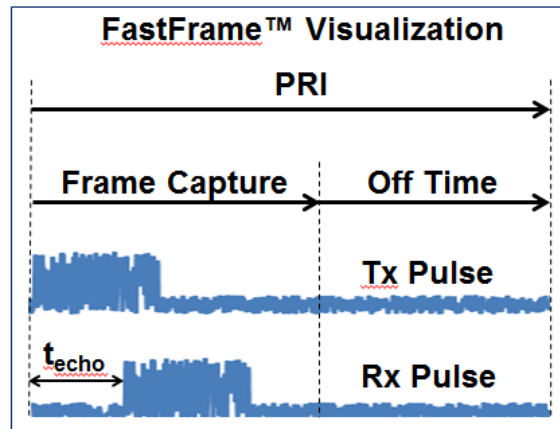


Figure 5. Oscilloscope Fastframe(TM) visualization

noise in between pulses [1, 10]. With one channel dedicated to the pulse trigger, the oscilloscope is capable of sampling up to three receiver chains allowing for multi-static expansion. The data are manually passed to the laptop which uses another Matlab

GUI to synthesize an image.

2.2.1.4 Antennas.

The system uses AirMax AM-2G16-90 antennas for transmit and receive functions which have a frequency range of 2.3 - 2.7 GHz. The transmit antenna is mounted on a stationary tripod and is manually pointed at the center of the target scene to achieve maximum available power on target.

The receive antenna is mounted on a track which allows linear movement controllable through a software interface. The forward beam width exceeds 60° with less than 3 dB attenuation at the extremes [11]. This characteristic is important in validating the spotlight mode processing assumption of Chapter I.

2.2.2 Laboratory Modifications.

The current iteration of the AFIT RAIL system is an improvement over multiple past research efforts [1, 7]. A complete description of system modifications and research methodology is outlined in this section. All laboratory equipment and research activities are located in AFIT's RAIL laboratory. Figure 6 shows the new configuration of the system hardware used in this research effort. The receive path antennae are mounted on moving tracks, or "rails", enabling linear movement during collection. The effects of a specific location and movement of receive antennae will be analyzed in later sections.

2.2.2.1 Matlab GUI Development.

The new GUI functions similarly to the system developed in [1–3]. The oscilloscope control function required updates to permit multiple receive channels for multi-static operation.

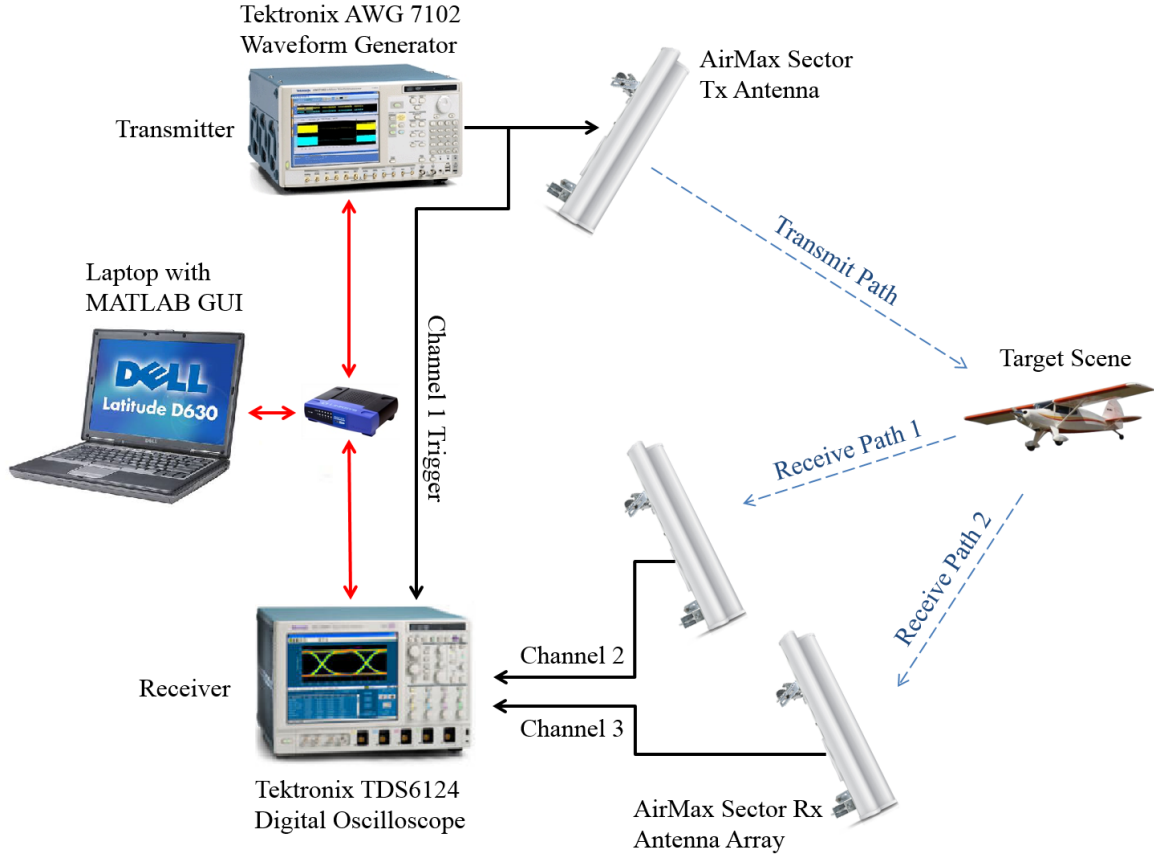


Figure 6. RAIL laboratory configuration

For data post-processing, the *passive radar toolbox* required extensive updates to facilitate equipment calibration, background subtraction, and autofocusing enhancements (discussed in Chapter III).

2.2.2.2 Linear Tracks.

Receiver antenna movement is facilitated by two linear tracks capable of traversing a 1.92 m aperture. The original track is a commercial, motorized product that interfaces with Matlab. This track continues to be used in its original configuration. The second track was developed in the AFIT RAIL and is driven by a series of pulleys and cables connected to the motorized track. In Figure 2(a) the commercial track can be seen behind the receive antenna on the left hand side and the AFIT-developed

track is on the right side.

Through the control interface, motors can move the commercial track (and by extension, the AFIT-track) at user-defined speeds up to approximately 0.6 m/s. Notably, the control interface does not provide real-time position information. Therefore, once receiver motion commences, position data is not available until motion has ceased and the user has manually requested a position update. In the context of SAR data collections taken while the receiver is in motion, all position data must be estimated from motion parameters. Invariably, this will introduce MMEs into data collections. The effect of these MMEs on SAR image formation is demonstrated in Section 2.6.

2.2.2.3 Targets.

Two target types and multiple scene geometries are analyzed to deduce the effect of RCS, distance, and angular separation on system performance. Targets were large metallic cylinders 15 cm in diameter with heights of 210 cm and 61 cm, as shown in Figure 7.

The monostatic RCS of a cylinder is approximated by $\sigma_{cyl} = \frac{2\pi a}{\lambda} l^2$ where a is the radius of the cylinder and l is the length [12]. Using a center frequency of 2.5 GHz, the large cylinder has a monostatic RCS of 17.3 m² and the small cylinder has an RCS of 1.5 m². The difference in energy reflected by these two targets is apparent in the images discussed later. Actual reflections will be based on a slightly smaller RCS because of the bistatic angle.



Figure 7. Metal cylinders used as radar targets

2.3 Laboratory Design Tradeoffs

2.3.1 Sampling Rate Study.

Experimental parameters may be generated based on the limited oscilloscope memory capacity of 64 mega-samples per channel and design of the receive antenna rail. The maximum practical rail speed is $v_{R_x} = 0.3$ m/s, and the rail length is $D = 1.92$ m. The resulting time required for a real-time collection ($t_{\text{collection}}$) is given by

$$v_{\text{Rx}} = \frac{D}{t_{\text{collection}}} \quad (1)$$

$$= \frac{D}{P \cdot \text{PRI} + t_{\text{echo}}} \quad (2)$$

where D is the distance traveled along the rail (which is also the synthetic aperture length), P is the number of pulses, t_{echo} is the time required for the pulse to travel from the transmitter to the receiver via the target, and PRI is the pulse repetition interval (PRI). Based on the physical side of the RAIL laboratory, t_{echo} is always less than $1\mu\text{s}$, which causes the P and PRI terms to dominate the expression.

Using $P = 16$ pulses as previous researchers commonly used [3, 7–9], a pulse repetition frequency (PRF) of ≈ 5.15 Hz is required to use the full length of the antenna synthetic aperture. This is far less than a typical PRF of > 1 kHz employed by most real-world systems [13, Table 2.1] but is necessary because of memory limitations. In future iterations of the radar system, frequency downconverting would allow for a lower sampling rate enabling more pulses to be collected across the aperture.

2.3.2 Waveforms.

An OFDM signal transmits information on N mutually orthogonal subcarriers simultaneously. Institute of Electrical and Electronics Engineers (IEEE) standard 802.16-2009 defines three-layer configurations using one, 256, and 2048 subcarriers [14]. Typically in radar processing, the received signal is compared against the transmitted signal in a matched-filter process.

To facilitate comparison with previous thesis results, a type of OFDM signal known as a Digital Audio Broadcasting (DAB) waveform is used through this research effort using a center frequency of $f_c = 2.5$ GHz, a bandwidth of $B = 300$ MHz, and

pulse width of $17 \mu\text{s}$. Notably, these characteristics are not strictly representative of OFDM standards, but were derived from equipment limitations. Previous research has shown this to be a valid scaling of signal parameters [3].

A Matlab *passive radar toolbox* was created through the analysis conducted in [3] to generate waveforms with desired characteristics and collect repeatable experimental data. For the purposes of this analysis, a DAB waveform will be used in conjunction with a refined and updated version of the Matlab passive radar toolbox.

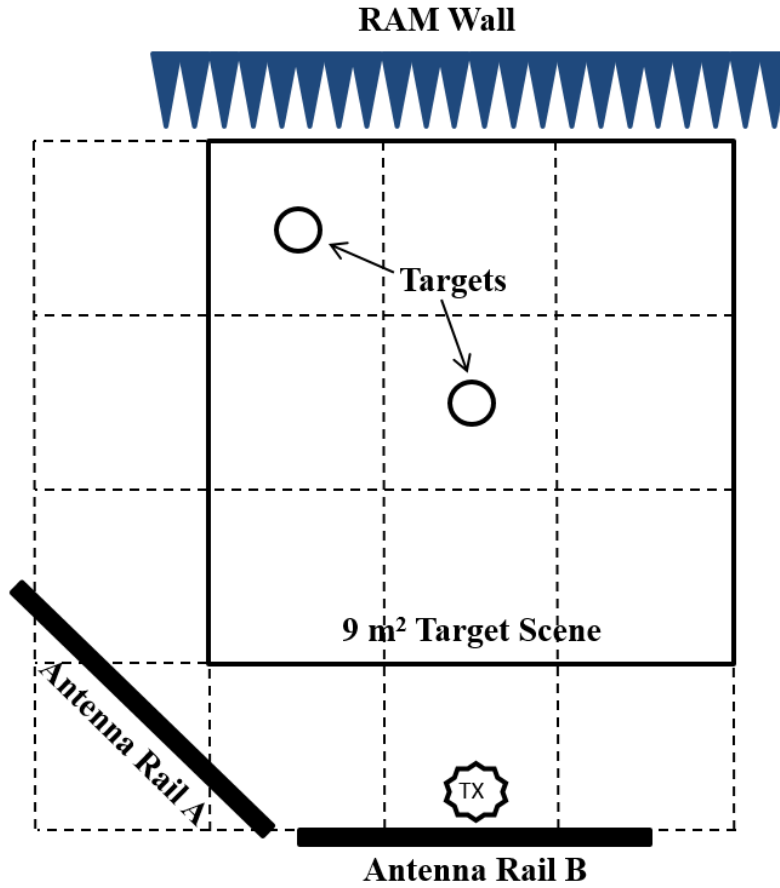
2.4 Laboratory Design Challenges

2.4.1 Scene Geometry.

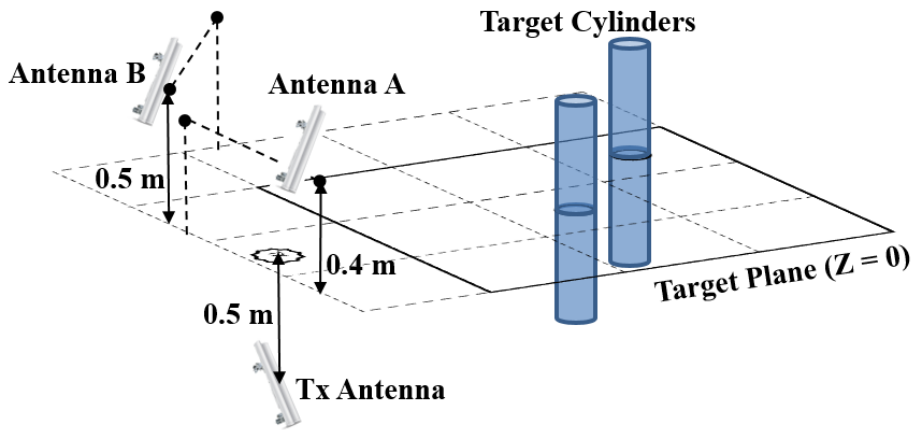
The physical size of the RAIL laboratory limits the target scene size to 3 m in range and 3 m in azimuthal distance. Validation and calibration data collection will employ a single target centrally located. In this configuration, resolution is large compared to scene size so no more than two targets are used in the scene simultaneously. Resolution will be discussed in more detail in Section 2.5.5.

Figure 8 shows a typical scene configuration including the location of the antenna rail tracks, transmitter, scene grid, and potential target locations. In this figure, target A is located at scene center. Many metallic objects are located around the laboratory outside of the scene grid but accurate scene images can be processed with data collected in this configuration.

Passive bistatic and multi-static signal processing are considerably more complex than the monostatic case. The developers [3, 7–9] of AFIT’s Matlab-based *Passive Radar Toolkit* used a North-referenced coordinate system to describe bistatic scene geometry (Figure 9) where R_T is the range from the transmitter to the target, θ_T is the transmitter look angle measured from the North reference, R_R is the range from the receiver to the target, θ_R is the receiver look angle measured from the North



(a) Two-dimensional image scene including antenna rail position and example target configuration.



(b) Three-dimensional image scene demonstrating location of transmit and receive antennas relative to reference plane.

Figure 8. Scene configuration in laboratory

reference (in Figure 9 this is a negative angle), L is the bistatic baseline (or distance between the transmitter and receiver), and β is the angle between the transmitter and receiver.

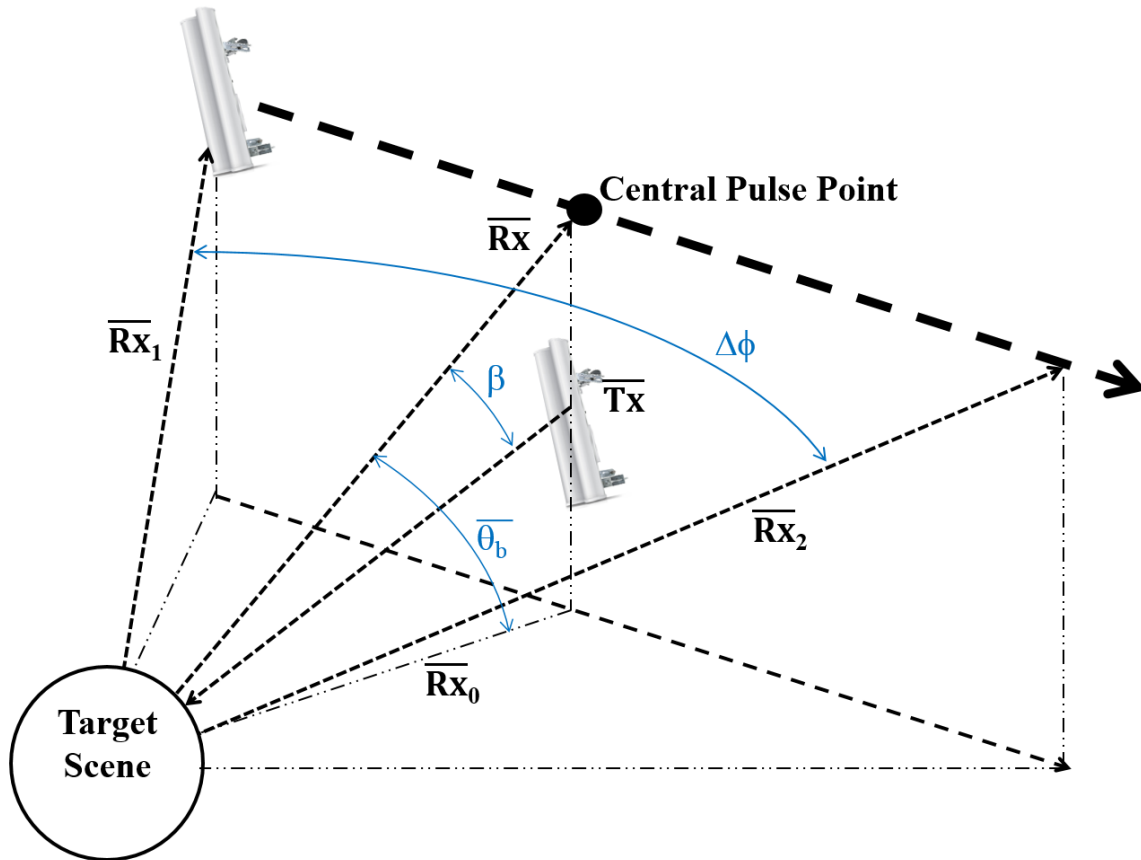


Figure 9. Bistatic scene geometry

2.4.2 Wave Curvature Analysis.

Though RF waves radiate spherically, for many long-range SAR systems a planar-wave (or far-field) assumption greatly simplifies computational complexity. Two criteria govern the the suitability of the far-field approximation [15]:

1. The range error caused by wavefront curvature across the scene must be less than a resolution cell such that range errors do not push target returns into neighboring range bins.

2. Range error must not exceed a small fraction of wavelength across all look angles.

Analysis completed in [1] has determined that the laboratory measurements conducted herein must be processed using near-field techniques. Such techniques are built in to the Matlab *passive radar toolbox*.

2.4.3 Data Generation and Analysis.

Once raw RF data samples are collected by the oscilloscope and manually saved to the laptop computer, individual pulse data is analyzed by a modified software suite. In previous versions, this software package was specific to bistatic scenarios. This thesis modifies the bistatic software to the multi-static case by summing the results as discussed in Section 2.5.3. Calculation of phase history and range profile data is critical to the calibration and focusing schemes discussed later. The processing software was written in a prior research effort and a complete mathematical description is found in [2].

In the original software version, phase history and range profile data are populated but internal system delays cause the scene center to appear offset to $Range = 0$ on the range profile axis. A means of calibrating the scene center to the center of the range profile axis is necessary for accurate imaging.

2.4.4 Calibration.

Theoretical SAR configurations assume pulse transmissions are generated at the transmit antenna and sampled at the receive antenna. In physical reality, pulse transmissions are generated in the AWG and pass through a low noise amplifier and 5 m of cable before reaching the antenna. Likewise, reflected signals are received by the antenna and travel through another 5 m of cabling and a low noise amplifier

before being sampled by the oscilloscope. In all configurations, the distance to the nether regions of the target scene is less than 5 m from the antenna. Equipment delays are greater than bistatic path delays and must be calibrated out of the system.

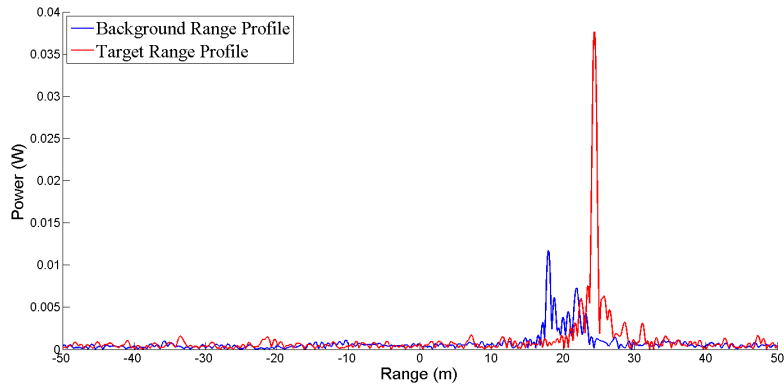
One of the first steps in data post-processing involves calculation of phase histories and range profile data for each individual pulse. Sample lengths are longer than pulse lengths and raw range profiles have an x-axis length of 100 m. To process a 3 m scene from a 100 m range profile, the user must know where the scene exists on the range profile. Previous research efforts used a single calibration constant determined through “guess and test” to shift the range profiles appropriately.

The new *passive radar toolbox* uses a calibration algorithm that compares a data collection of an empty scene (background) against a data collection of a scene with a large target located at scene center. Range profile data is generated through a matched filter against the transmitted signal and rearranged so that the scene center is the first point in the range profile data vector. This is accomplished using the estimated target and receiver position solutions and has the effect of removing the distance from the receiver to the target (which varies pulse to pulse) from the range profile data.

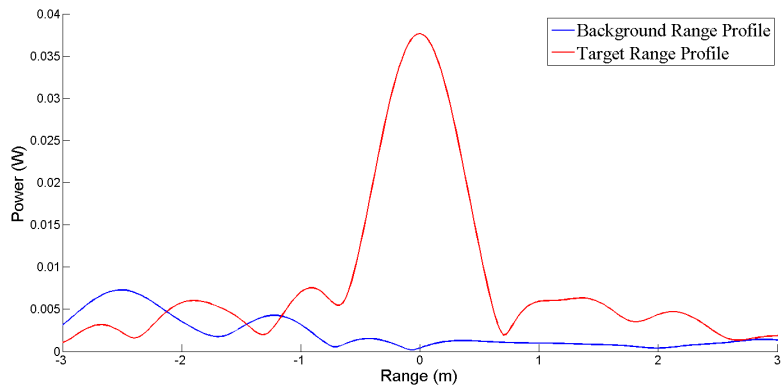
Because the range profile axes for each pulse are now aligned, the calibration algorithm sums the range profiles from each pulse, resulting in a single plot spanning the entire range profile axis. The summed range profile is compared against a background measurement to determine target location along the axis. The calibration scene is setup with a single target at scene center, so the displacement of the range profile’s target spike from the origin is becomes the calibration factor.

Figure 10(a) shows this summed range profile plot for both the target and background data after the calibration factor has been applied. As expected, the target data (red) contains large spikes where the data was highly correlated. At this same

location, the background data has very little correlation. Notably, there is also a large spike in background correlation at an x-axis location of 5 m, but this is outside the target scene. This spike was present in many background collections and is attributed to other reflective objects in the laboratory. Figure 10(b) zooms in on the target scene location in the range profile and shows what is likely the location of the target at $Range = 0$. The target scene extends from $Range = -1.5$ to $Range = 1.5$.



(a) Range profile comparison before calibration shows target reflections are found 25 meters away from scene center



(b) Range profile calibrated and zoomed in to show scene center target reflection

Figure 10. Range profile difference between scene with large target and scene with no target

The calibration algorithm observes the range location of the target spike and determines a calibration value applicable to all range profile data to effectively move

the target spikes over the location where $Range = 0$, or scene center. This calibration scheme is applied to all receive paths and all data processed past this point have appropriate calibration values applied.

2.5 Methodology

2.5.1 Data Collection.

SAR data is collected in one of two ways: *stripmap*, as illustrated in Figure 11(a), or *spotlight*, as shown in Figure 11(b). Stripmap imaging implies the receive antenna is traveling a relatively straight course with the receive antenna pointing at a fixed angle, enabling a long strip of ground to be imaged. In spotlight imaging, as the platform moves, the antenna pointing angle is adjusted in the direction of target center. Alternatively, the path of the platform can be curved, so that a fixed antenna would point at a stationary target. Spotlight imaging allows for higher resolution of a smaller target area [5], while the stripmap technique images a large target area but with poorer resolution [15].

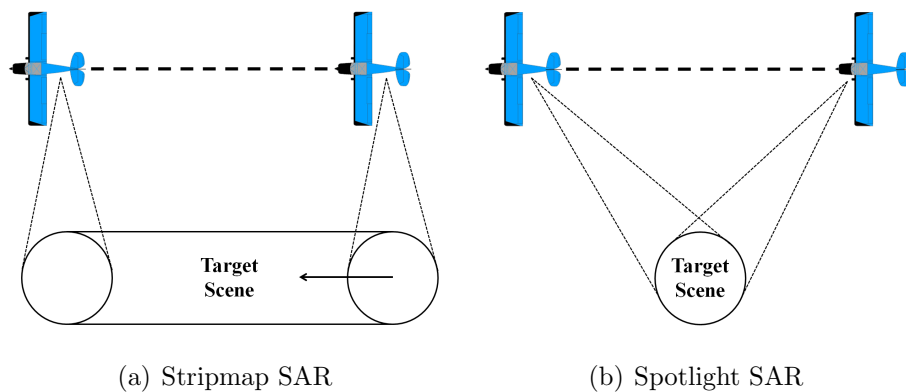


Figure 11. Comparison of SAR imaging techniques

The AFIT SAR system employs spotlight image processing even though the physical configuration appears stripmap. There are complex methods for processing stripmap data using spotlight algorithms [16]; however, the configuration of the

AFIT system allows for the assumption that spotlight and stripmap modes are geometrically interchangeable. Specifically, if all scene features fall within the antenna beamwidth for the entire azimuthal extent of the data collection, the spotlight and stripmap processing modes yield the same results. All data collections made in support of this thesis used configurations which kept targets within the -6 dB beamwidth of the receive antennae as derived from manufacturer specifications. Figure 12 shows a worst-case scenario scene geometry. In this scenario, the receiver antenna is at the far extent of its travel to the right, while the target is in the lower left corner. Nevertheless, the target remains within the antenna beamwidth.

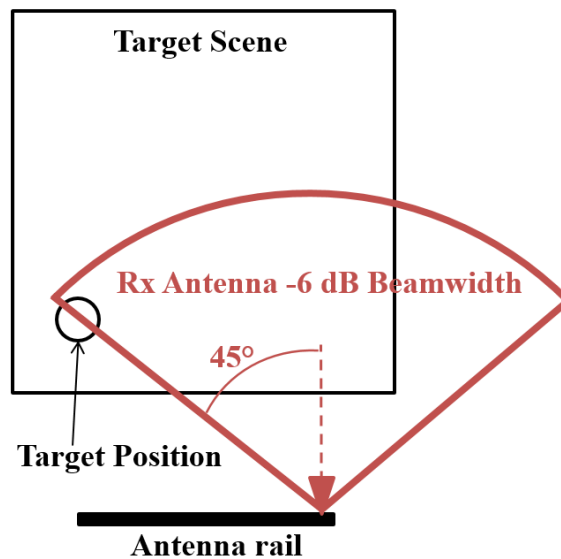
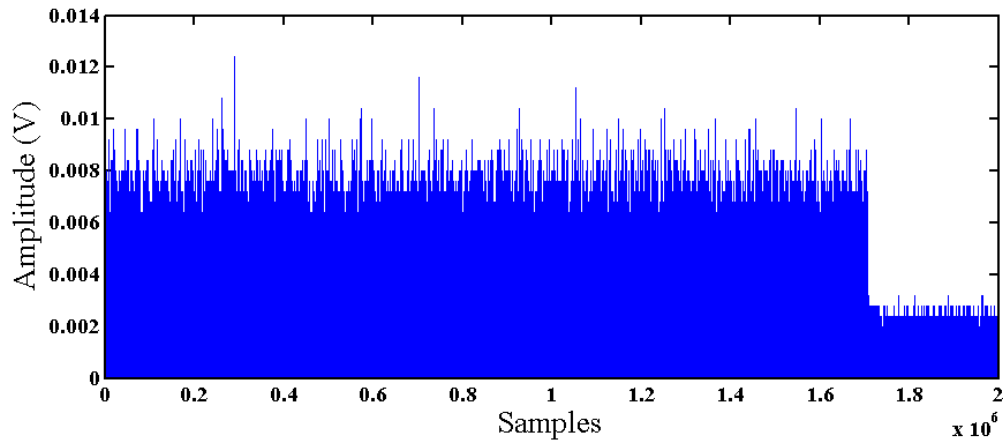


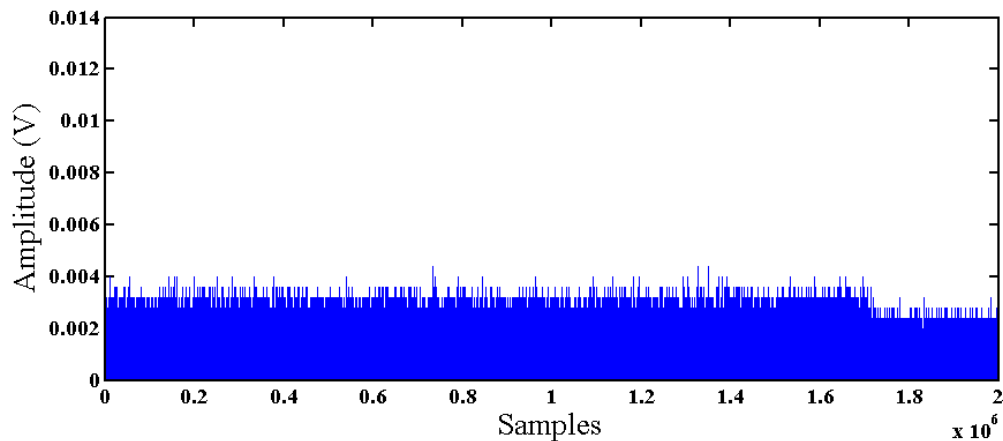
Figure 12. Overlay of AirMax antenna beamwidth on worst-case scenario scene geometry.

For the purpose of this thesis, antenna beamwidth is defined as -6 dB. To verify this assumption, Figure 13 compares a pulse sampled from the rail position where the antenna gain is estimated at -6 dB to a background pulse (no target present). The large difference in target return amplitude demonstrates that sufficient reflections are collected by the radar in the worst-case scenario of Figure 12 and the assumption that spotlight processing techniques are applicable to data collected by this stripmap

system is deemed valid.



(a) Sampled pulse from right side of Antenna B aperture with a target present at the -6 dB beamwidth location.



(b) Sampled pulse from right side of Antenna B aperture with no target present in the scene.

Figure 13. Comparison of Antenna B pulse amplitudes with a target at (-1,-1) from right side of aperture where gain is -6 dB and a background collection with no target present

2.5.2 Image Processing.

After calibration values have been determined, the data collected from the oscilloscope is passed to the *passive radar toolbox* where the phase history is populated by matched filtering against the full reference signal.

Once the phase history is populated, the data is passed into an image formation

algorithm. The most common algorithms are polar reformatting, range migration, and convolution backprojection (CBP) [2–4]. Previous developers opted for a filtered backprojection rather than CBP for purposes explained in [1]. With Figure 8 in mind, the image processing algorithm generates a two-dimensional (2D) image of the scene. Figure 14 is a SAR image (generated from simulated bistatic phase history data received on Antenna B from a point target) overlaid on the lab scene to demonstrate the ultimate product of AFIT’s SAR imaging system.

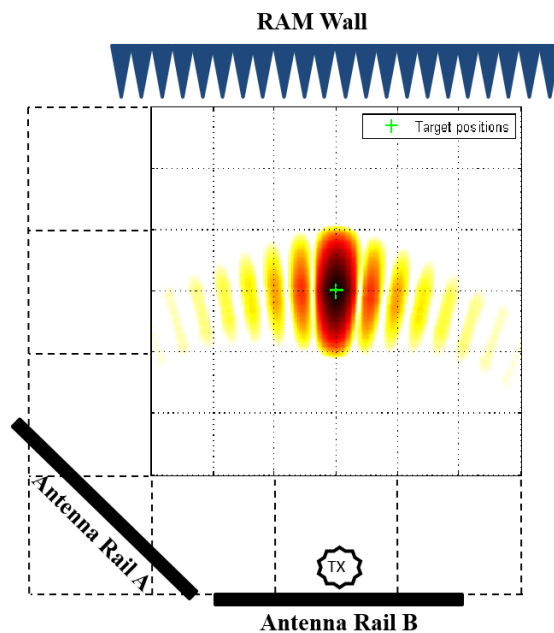


Figure 14. SAR image overlaid onto laboratory environment.

2.5.3 Multistatic Imaging through Coherent Summation.

To perform multi-static image processing, images are first calculated from each transmitter and receiver combination using a backprojection algorithm (BPA). The pixel matrix from each bistatic combination is coherently summed to deduce amplitude and phase. Pixel intensities are magnitudes based on spatial orientation, roughness, and the dielectric constant of the target surface [12].

Each transmitter/receiver pair is analyzed individually and the results are summed across the target matrix to generate a multi-static image. Thus, data collections occur using bistatic scene geometry and are post-processed into a multi-static solution as shown in Figure 15.

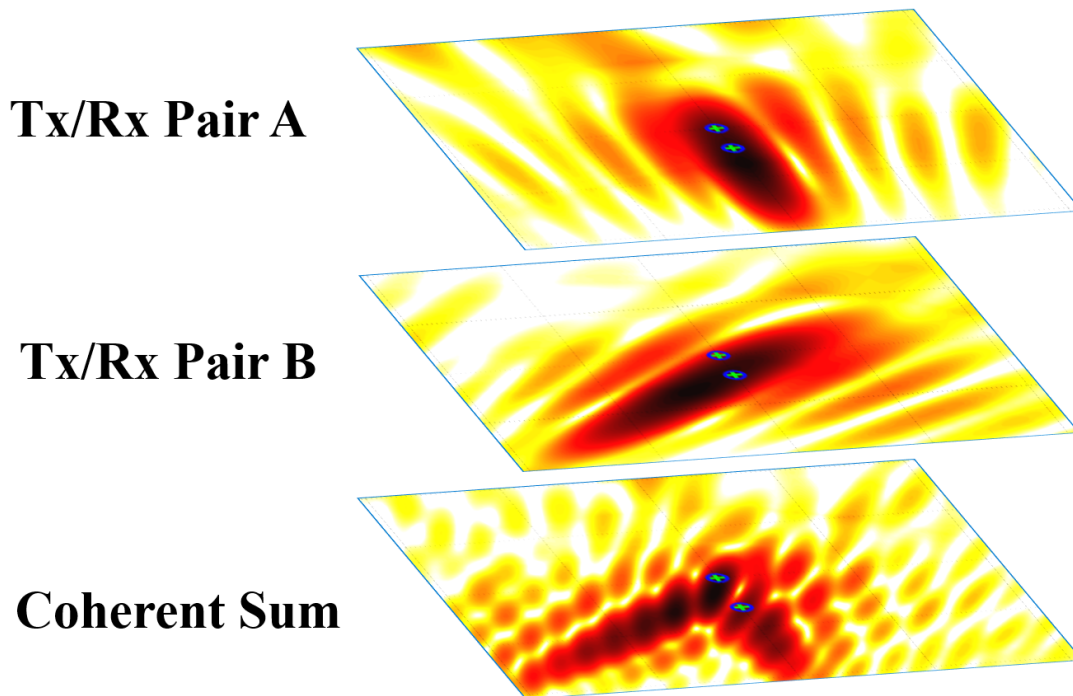
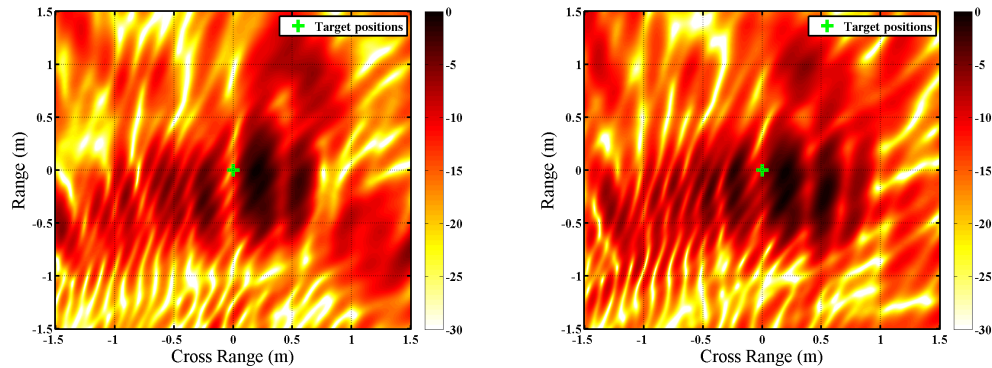


Figure 15. Multistatic image coherent summation

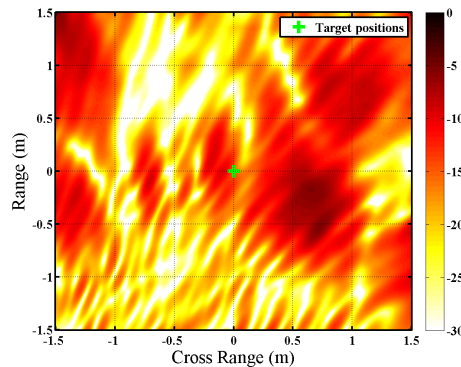
2.5.4 Extended Aperture Image Processing.

Another method of combining phase histories from two different receive antennae involves concatenating the collections as if a single antenna traversed both linear tracks. Though this method does not employ true multistatic processing, it has the effect of lengthening the synthetic aperture and increasing the resolution performance compared to the bistatic case on a single linear track. In theory, there is no difference between this type of processing and multistatic image summation. However, when position errors are present and autofocusing is applied, a difference can be realized.

Figure 16(a) shows an image created through extended aperture image processing and compares it to an image created via multistatic summation. The extended aperture image contains weaker side-lobes compared to the multistatic summation in 16(b). The full difference between these two images is plotted in 16(c). This processing technique is discussed further in Chapter IV.



(a) Image created using concatenated collection runs. (b) Image created using multistatic summation.



(c) Difference plot of images created using the various multistatic techniques.

Figure 16. Comparison of SAR multistatic synthesis techniques

2.5.5 Resolution.

In the context of imaging radar, resolution refers to a system's ability to differentiate (or resolve) between two features in the region of interest. Figure 17(a) shows two point targets spaced 2.5 m apart in a simulated SAR collection. The associated

target blobs show two distinct targets are present in the scene. Figure 17(b) shows the same two targets with 1 m spacing. The target blobs are now merged, making it difficult to determine how many targets are present. Specifically, resolution is a measure of the minimum possible distance between two points that the radar can differentiate between [5].

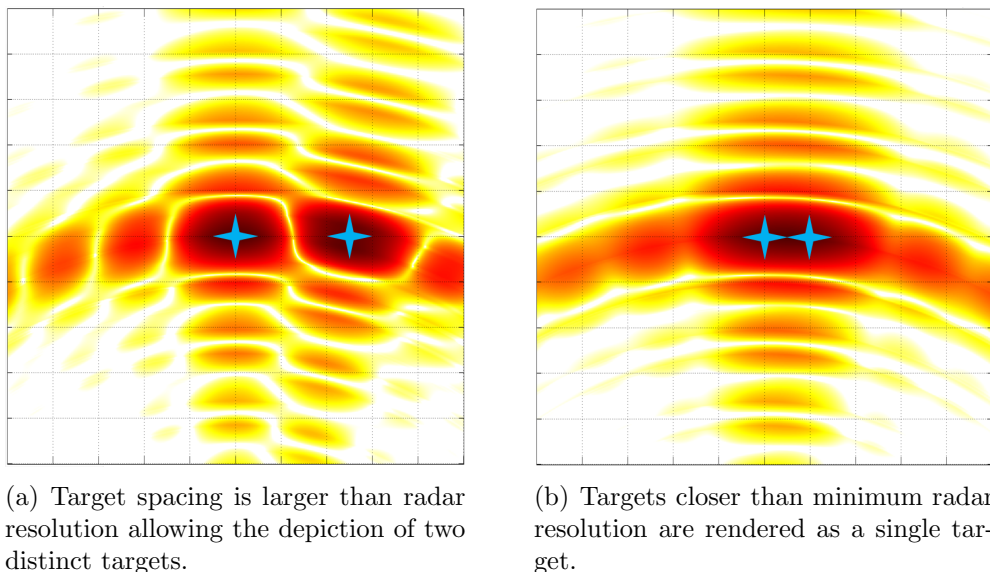


Figure 17. Illustration of SAR resolution

Monostatic resolution is inversely proportional to bandwidth and is specified in range as $\rho_x = \frac{c}{2B}$ and in azimuth as $\rho_y = \frac{\lambda}{2\Delta\phi}$. The speed of light is given by c in m/s, B is the signal's bandwidth in Hz, λ is the signal's wavelength in meters at the center frequency, f_c , and $\delta\phi$ is the collection angular extent in radians, or angular diversity of the flight path. An isotropic point scatter induces a sinc function in the receiver, and the resolution parameters measure the distance from the center to the first zero crossing of this response.

In the monostatic case, resolution is improved as wavelength decreases but shorter wavelengths are also victims of attenuation by atmospheric features. In the bistatic case, resolution is also dependent on the angular separation of the transmitter and

receiver from the target in addition to frequency [17, Ch. 10]. The following mathematical development assumes a small imaged scene relative to bistatic range (far-field assumption) but is useful for estimating bistatic resolution in a near-field laboratory environment.

All data collections conducted in support of this thesis used the same equipment configuration so the following resolution analysis applies. Bistatic resolution in the range direction is defined by

$$\rho_y = \frac{c}{2B \cos(\beta/2)} \quad (3)$$

where β is the three-dimensional half-bistatic angle between the transmitter and receiver at the center pulse position measured from scene center. For antenna rail configurations shown in Figure 8, the half bistatic angle (depicted in Figure 9) is

$$\beta = \cos^{-1} \left(\frac{(\vec{T_x} \cdot \vec{R_x})}{|\vec{T_x}| |\vec{R_x}|} \right) \quad (4)$$

where the vectors from scene center to the transmitter and receiver at the central pulse are denoted as $\vec{T_x}$ and $\vec{R_x}$ respectively. Resulting bistatic angles are $\beta_A \approx 0.8572$ radians and $\beta_B \approx 0.3172$ radians for antennas A and B.

Bistatic resolution in the cross range direction is more complex, but can be simplified by projecting three-dimensional (3D) resolution into the ground plane, resulting in

$$\rho_x = \frac{c}{2B \cos(\beta/2) \cos(\bar{\theta}_b)} \quad (5)$$

where $\bar{\theta}_b$ is the elevation of the bistatic look angle [3, 17]. The bistatic look angle is approximately the vector that bisects the vectors to the transmit antenna and the

receiver antenna center pulse. The bisect look angle vector is

$$f_x = \frac{f}{2}[\cos(\phi_t) \cos(\theta_t) + \cos(\phi_r) \cos(\theta_r)] \quad (6)$$

$$f_y = \frac{f}{2}[\sin(\phi_t) \cos(\theta_t) + \sin(\phi_r) \cos(\theta_r)] \quad (7)$$

$$f_z = \frac{f}{2}[\sin(\theta_t) + \sin(\theta_r)] \quad (8)$$

where ϕ is the the measured azimuth and θ is the measured elevation angles of the transmitter ($_t$) and the receiver ($_r$). The elevation of the bistatic look angle, $\bar{\theta}_b$, is

$$\bar{\theta}_b = \tan^{-1} \left(\frac{f_z}{\sqrt{f_x^2 + f_y^2}} \right), \quad (9)$$

resulting in $\bar{\theta}_A \approx 0.7678$ radians and $\bar{\theta}_B \approx 0.3172$ radians for antennas A and B.

Finally, scene resolution (Table 1) is determined using known signal parameters, $B = 300$ MHz, $\lambda = c/f_c \approx 0.12$ m.

Table 1. Calculated Scene Resolution

Axis	Antenna A	Antenna B
ρ_x	0.76 m	1.06 m
ρ_y	0.55 m	0.51 m

Due to blurry images attributed to error sources, it is difficult to observe resolution effects on the SAR images. Further analysis of resolution achieved in experimental and simulated data sets can be found in Chapter IV.

2.6 Error Sources

A SAR data collection requires sampling of amplitude and phase of a return signal. Phase errors are intrinsic to real-world data sampling and result from position uncertainty of the transmitter and receiver, signal propagation effects, source coherence,

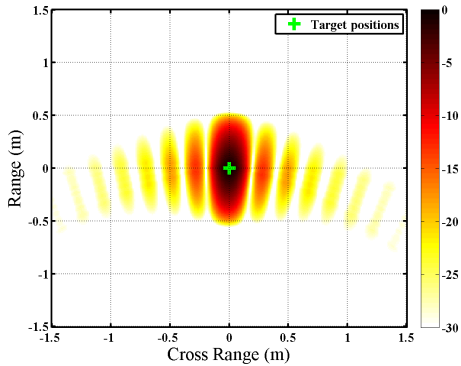
and internal system delays [16]. Their net result is distortion in the reconstructed image which hampers interpretation. The effects of MMEs on SAR image quality are examined in this section. Focusing techniques used to mitigate these errors are discussed in Chapter III.

As discussed earlier, the receiver antenna position must be estimated from a velocity vector and cannot be measured directly. Thorough analysis conducted through a previous research effort [1] determined the net position error would not likely exceed $\bar{y}_i \approx 0.3$ m in the downrange direction and $\bar{x}_i \approx 0.6$ m in the cross range direction. Errors of this magnitude are not likely on the current system, but will be used in worst-case scenario analysis.

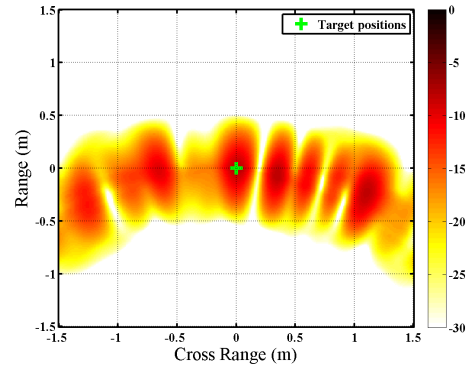
Figure 18(b) is a SAR image generated with the *passive radar toolbox* which incorporates random position errors not exceeding the stated amount. Compare this to the same phase history data with no position error applied (Figure 18(a)) and phase history data experimentally collected in the laboratory resulting in the image shown in Figure 18(c).

The experimental image clearly exhibits characteristics attributed to position errors, though other blurring phenomena are also present. Since these errors manifest themselves as random quantities applied to each pulse individually, they cannot be solved for. However, they can be estimated and removed from the data through the optimization algorithm described in Chapter III.

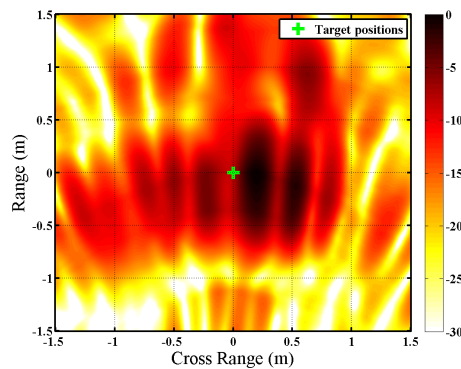
While most collections made in the course of this research employed receiver antennas in constant motion, the radar controller software is capable of collecting data in a “move-stop-move” fashion where the antenna only moves between pulse receptions and remains stationary during reception. In this case, the antenna is commanded to the appropriate position along the linear track with a margin of error that is less than 1 mm. This collection methodology eliminates significant position error (though



(a) Simulated SAR image created using ideal receiver position vector.



(b) Simulated SAR image with random position errors of $\bar{y}_i \leq 0.3$ m in the downrange direction and $\bar{x}_i \leq 0.6$ m in the cross range direction applied.

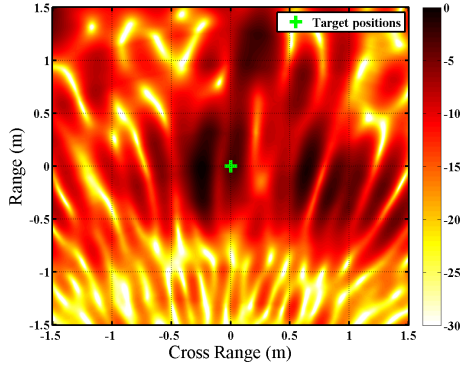


(c) SAR image generated from phase history data collected in laboratory.

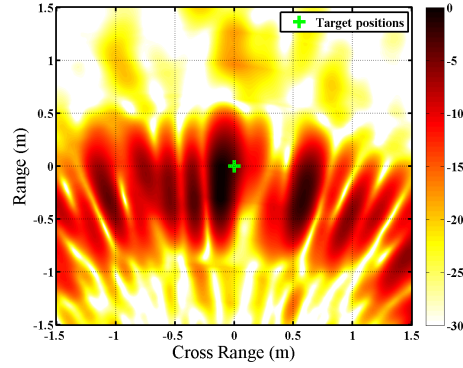
Figure 18. Effects of position error on simulated and experimental phase history data.

measurement error still applies) but takes approximately 30 minutes per collection because of interface speeds across the network, compared to five minutes per collection for moving collections. Figure 19 compares a collection made using a moving antenna to a collection made using the “move-stop-move” approach, demonstrating the effects of smaller position errors on image quality.

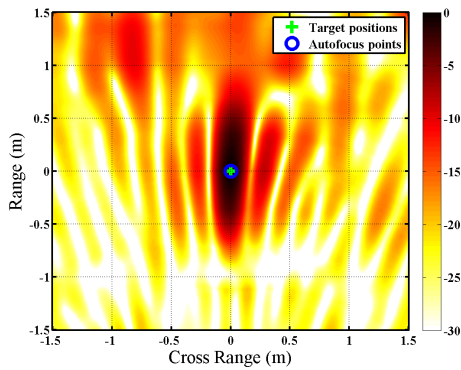
The contrast between Figure 18(b) and Figure 18(c), and Figure 19(a) and 19(b) indicates other sources of error are causing image degradation. Figures 19(c) and 19(d) are images resulting from applying the autofocus algorithm (discussed in Chapter III) to 18(b) and 18(c). Comparing to the simulated scenario in Figure 18(a),



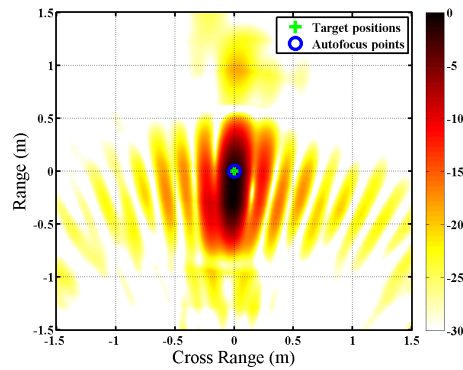
(a) Experimental moving collection with a target at scene center.



(b) Experimental “move-stop-move” collection with target at scene center.



(c) Experimental moving collection from (a) with autofocusing applied.



(d) Experimental “move-stop-move” collection from (b) with autofocusing applied.

Figure 19. Image quality is improved using when pulse reception occurs while antenna is stationary such as in the “move-stop-move” scenario.

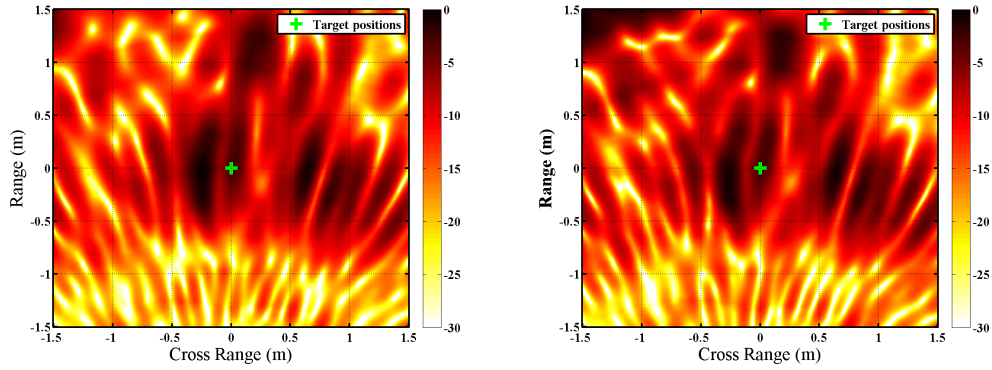
the partial removal of position errors has a significant effect on image quality. The following list acknowledges potential candidates, though most are not analyzed in this thesis.

- All simulation and data post processing have assumed targets are point targets at exact locations. In reality, reflections from the actual cylindrical targets will vary somewhat from theoretical reflections from point targets. This will affect resolution measurements as physical targets will create larger blobs in the images than the theoretical targets.
- The cylindrical targets must occupy space, such that their placement in the

scene is not confined to a single coordinate. The actual range to the target is therefore offset by a certain amount depending on receiver antenna location.

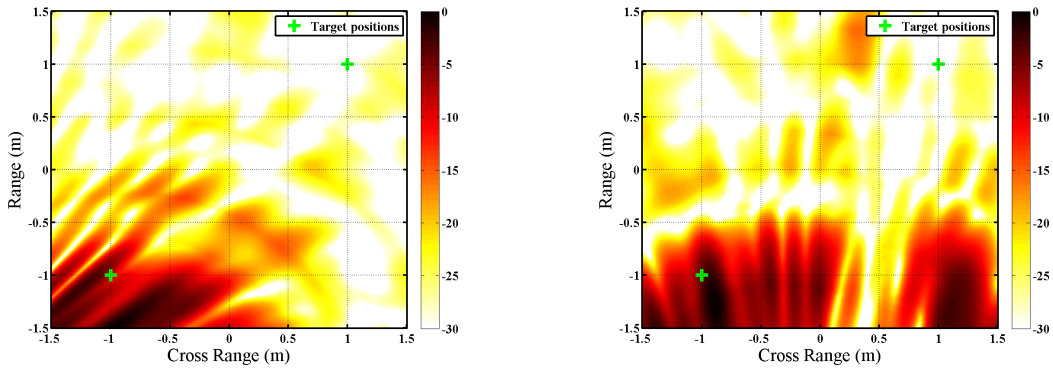
- All target and antenna locations were measured using a low-budget measuring device. Measurement error from human factors is unavoidable using this technique; therefore, more position and range errors exist in the data than are specifically accounted for. Some of these, however, are mitigated through the autofocusing techniques discussed in Chapter III.
- For scenes containing two targets or targets near scene edges, multi-path effects can create additional target peaks in images. These effects are not analyzed in this research.
- The laboratory scene was empty except for targets, however multiple reflective objects are located in the lab. Clutter from these objects could contribute to image degradation. Background subtraction was applied to imaging results from collections made with a target at scene center and Figure 20 compares this image to the original. Despite the some differences, background subtraction has trivial benefit in distinguishing target locations for unfocused images. Therefore, no background subtraction is used in any other figures throughout this thesis.

The necessity for position error compensation is illustrated by the blurry SAR images in Figure 21. Out of over 100 data collections performed during the course of this research, the images in Figure 21 are the most user-friendly—that is, they give the user the best chance at determining the position of the target, despite multistatic imaging enhancements shown in 21(c). Clearly, position error mitigation techniques are necessary to achieve acceptable system performance. Chapter III applies an autofocusing algorithm to the phase history to improve image readability.



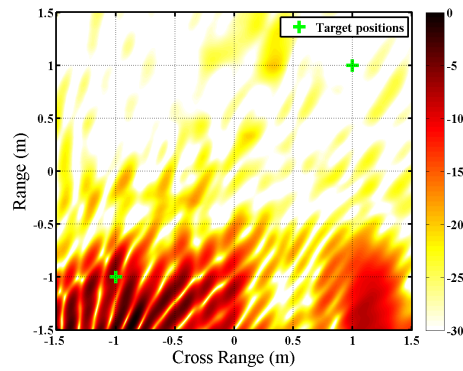
(a) Laboratory image before background subtraction. (b) Laboratory image after background subtraction.

Figure 20. Effects of background subtraction on laboratory SAR image.



(a) The best image processed from data received by Antenna A.

(b) The best image processed from data received by Antenna B.



(c) Multistatic image created from coherent sum of (a) and (b).

Figure 21. Example SAR images created using phase history with uncorrected position error.

III. Autofocusing Enhancements

3.1 Introduction

A SAR data collection requires sampling of amplitude and phase of a return signal. Phase errors are intrinsic to real-world data sampling and result from position uncertainty of the transmitter and receiver, signal propagation effects, source coherence, and internal system delays [16]. Their effects may be minimized through position error analysis and calibration techniques, but enhanced data processing can further refine image clarity. A semidefinite relaxation autofocus algorithm derived in [18] is discussed here and applied to the bistatic and multistatic RAIL scenes used throughout this research.

3.2 Background

Numerous autofocus algorithms have been proposed to enhance image reconstruction. The methods used here expand upon the semidefinite relaxation approach discussed in [19] but applied to CBP. This analysis will be applied to theoretical SAR data as well as experimental data collected in the RAIL.

The techniques posed here require *a priori* knowledge of areas of strong returns in an image. Specifically, target locations are supplied to the algorithm for image optimization. Thus, the technique is well-suited to laboratory measurements such as those with the AFIT SAR system.

3.3 Mathematical Modeling of Calibration and Position Error

This section provides a mathematical basis for calibration error and MME mitigation through focusing. The imaging scenario used in this analysis is depicted in Figure 22. The transmitter and receiver are assumed to be stationary during pulse

transmission and reception and the target scene is assumed to consist of stationary isotropic point scatterers with known position.

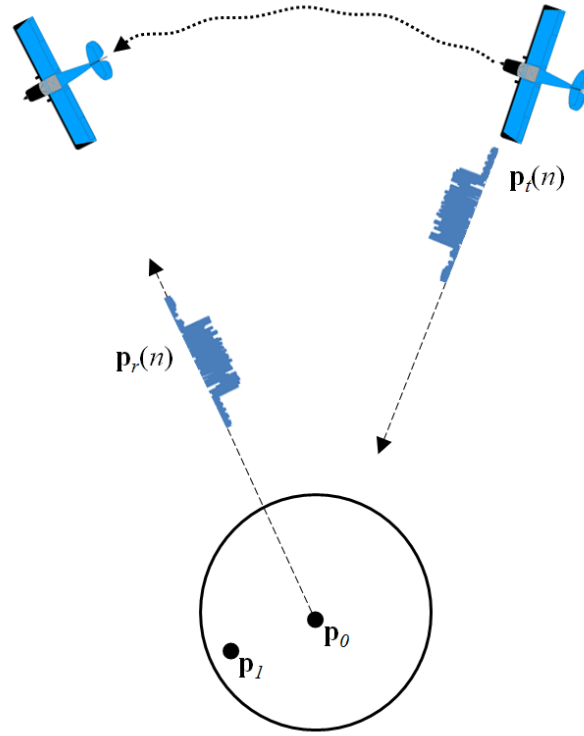


Figure 22. Spotlight mode SAR imaging scenario

Using a common signal model, the n th transmitted pulse is

$$u_n(t) = \text{Re} \{ u_n(t) e^{j2\pi f_c t} \}, \quad (10)$$

where u_n is the n th baseband transmitted pulse and f_c is the center frequency. Each scatterer, \mathbf{p}_i , within the scene reflects the i th echo return of the n th transmit signal. To simplify problem formulation and isolate error terms, this scenario will assume the scene contains a single, noise free scatterer, \mathbf{p}_1 . Results are easily expanded to a

complex scene. The echo return of the n th pulse from \mathbf{p}_1 is

$$s_{\mathbf{p}_1, n}(t) = \gamma_n \text{Re} \{ u_n(t) e^{j2\pi f_c t} \} \quad (11a)$$

$$= \gamma_n u_n(t - \tau_{\mathbf{p}_1}(n)) \quad (11b)$$

$$= \gamma_n u_n(t - \tau_{\mathbf{p}_0}(n) - \Delta\tau_{\mathbf{p}_1}(n)), \quad (11c)$$

where γ_n is a complex scaling coefficient for the n th pulse, $\tau_{\mathbf{p}_1}(n)$ and $\tau_{\mathbf{p}_0}(n)$ are bistatic delays to the scatterer, \mathbf{p}_1 , and scene center, \mathbf{p}_0 for the n th pulse, respectively, and $\Delta\tau_{\mathbf{p}_1}(n) = \tau_{\mathbf{p}_1}(n) - \tau_{\mathbf{p}_0}(n)$ is the differential delay relative to the delay to scene center of the n th pulse for the scatterer, \mathbf{p}_1 . Note the differential delay will be positive for a scatterer beyond scene center, and negative for a scatterer nearer than scene center. The generic bistatic delay of pulse n to a point \mathbf{p}_1 is

$$\tau_{\mathbf{p}_1}(n) = \frac{\|\mathbf{p}_1 - \mathbf{p}_t(n)\|_2 + \|\mathbf{p}_r(n) - \mathbf{p}_1\|_2}{c}, \quad (12)$$

where c is the speed of light and $\mathbf{p}_t(n)$ and $\mathbf{p}_r(n)$ are the ideal positions of the transmitter and receiver during the n th pulse. The graphic in Figure 23 shows the differential range to a point scatterer, \mathbf{p}_1 for the n th pulse.

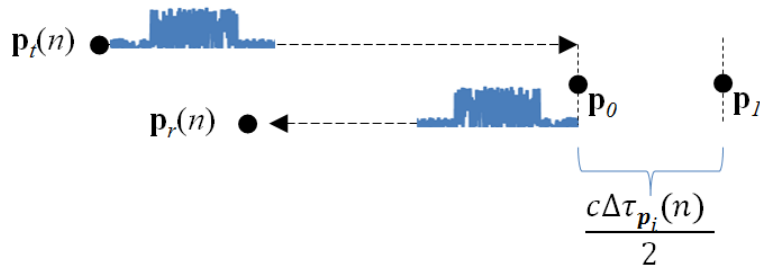


Figure 23. Differential range to a scatterer, \mathbf{p}_1 .

Because of the error sources discussed earlier, the ideal delay to scene center, $\tau_{\mathbf{p}_0}(n)$, inherits a position error term, $\delta\tau_{\mathbf{p}_0}(n)$, which is unknown to the user. In this

analysis, the error will be represented by uncertainty in the position of the receiver, resulting in phase errors that degrade the SAR image quality. The position error and resulting phase errors are unique to each received pulse.

The delay is also affected by an unknown calibration error, $\delta\rho_{\mathbf{p}_0}(n)$, resulting from equipment delay discussed in Section 2.4.4. This delay is assumed to apply equally to all pulses received by a specific receive antenna.

The ideal delay to scene center becomes an estimated delay of $\hat{\tau}_{\mathbf{p}_0}(n) = \tau_{\mathbf{p}_0}(n) + \delta\tau_{\mathbf{p}_0}(n) + \delta\rho_{\mathbf{p}_0}(n)$. The return echo observed at the receiver is mixed with a complex exponential delayed to scene center by the estimated delay, $e^{-j2\pi f_c(t - \hat{\tau}_{\mathbf{p}_0}(n))}$. The n th mixed return is passed through an ideal low-pass filter; the resulting complex representation of the received signal is

$$r_n(t) = s_{\mathbf{p}_1, n}(t) e^{-j2\pi f_c(t - \hat{\tau}_{\mathbf{p}_0}(n))} \quad (13a)$$

$$= \gamma_n u_n(t - \tau_{\mathbf{p}_0}(n) - \Delta\tau_{\mathbf{p}_1}(n)) e^{-j2\pi f_c(\Delta\tau_{\mathbf{p}_1}(n) - \delta\tau_{\mathbf{p}_0}(n) - \delta\rho_{\mathbf{p}_0}(n))}. \quad (13b)$$

Let $\mathcal{D}(\tau)$ become the delay-by- τ operator,

$$\mathcal{D}(\tau) = \mathcal{D}(\tau_{\mathbf{p}_0}(n) + \Delta\tau_{\mathbf{p}_1}(n) + \delta\rho_{\mathbf{p}_0}(n)) \quad (14a)$$

where $\delta\rho_{\mathbf{p}_0}(n)$ is the calibration factor applied from Section 2.4.4) which affects the signal delay resulting in

$$r_n(t) = \gamma_n u_n(t - \tau_{\mathbf{p}_0}(n) - \Delta\tau_{\mathbf{p}_1}(n) - \delta\rho_{\mathbf{p}_0}(n)) e^{-j2\pi f_c(\Delta\tau_{\mathbf{p}_1}(n) - \delta\tau_{\mathbf{p}_0}(n))} \mathcal{D}(\tau). \quad (15)$$

While the calibration factor is only an approximation, the focusing algorithm development drops the $\mathcal{D}(\tau)$ term altogether. The other occurrences of $\delta\rho_{\mathbf{p}_0}(n)$ are removed from the algorithm development because the approximate correction factor

takes place before autofocusing.

Further derivation details are available in [6, 18]. The algorithm’s inputs include estimated scene geometry, signal characteristics, and measured range profile data and the output is focused phase history data from which an improved image may be processed. The algorithm’s backbone is semidefinite relaxation and maximization of the objective function which requires *a priori* knowledge of the locations of strong scatterers in the scene. Clearly *a priori* knowledge of target locations is a limitation on the real-world implementation of this method.

3.4 Results from Simulation

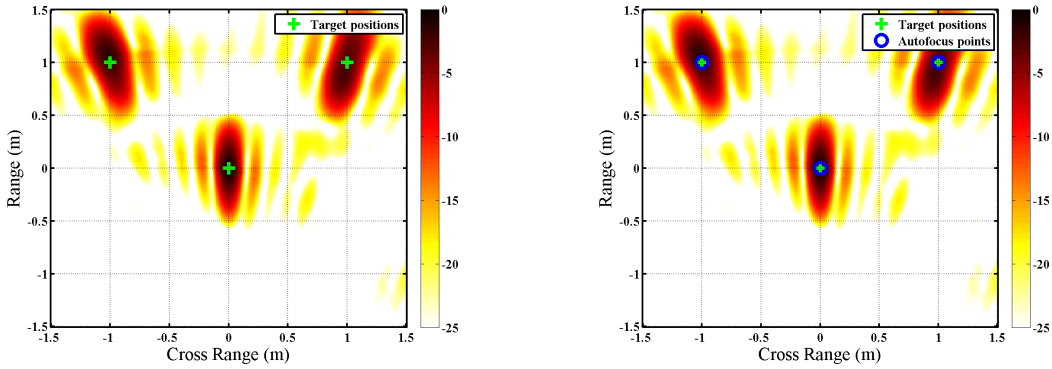
The near-field semi-definite autofocus algorithm described above was coded in Matlab as part of the analysis completed in [6, 6]. For this research effort, the code was first applied to simulated noise-free phase history data generated using scene geometry and equipment parameters representing AFIT’s RAIL configuration shown in Figure 8. The simulation first computes an ideal SAR image of the laboratory scene based on perfect knowledge of receiver, target, and transmitter position. It then applies a user-defined error into the receiver position which may be rotational or white noise error, and produces another image which appears significantly defocused due to the phase offsets induced by the position errors. Next, the simulation applies the focusing algorithm across the known target set, $\mathcal{T} = \{\mathbf{p}_A, \mathbf{p}_B, \mathbf{p}_C\}$, maximizing the image points corresponding to each target’s position. A final image is generated to show the focusing results. For comparison purposes, all SAR images are normalized by the same value and shown on the same scale. The receiver position vector describes 16 pulses along the linear track. The simulation uses a carrier frequency $f_c = 2.5$ GHz and a bandwidth $B = 300$ MHz.

3.4.1 Case I: No induced error.

In this case, the error term is set to zero to ensure the convex optimization faithfully reproduces the original image. Table 2 shows the peak magnitude for each of the targets in the ideal, defocused, and autofocused images. As expected, the peak target responses are identical in all cases. The plots in Figure 24 show that the ideal and images are indeed identical.

Table 2. Case I Peak Target Reflections

Target	Ideal Value	Defocused Value	Autofocused Value
A	-0.04 dB	-0.04 dB	-0.04 dB
B	-1.92 dB	-1.92 dB	-1.92 dB
C	-2.92 dB	-2.92 dB	-2.92 dB



(a) Simulated SAR image created using ideal receiver position vector.

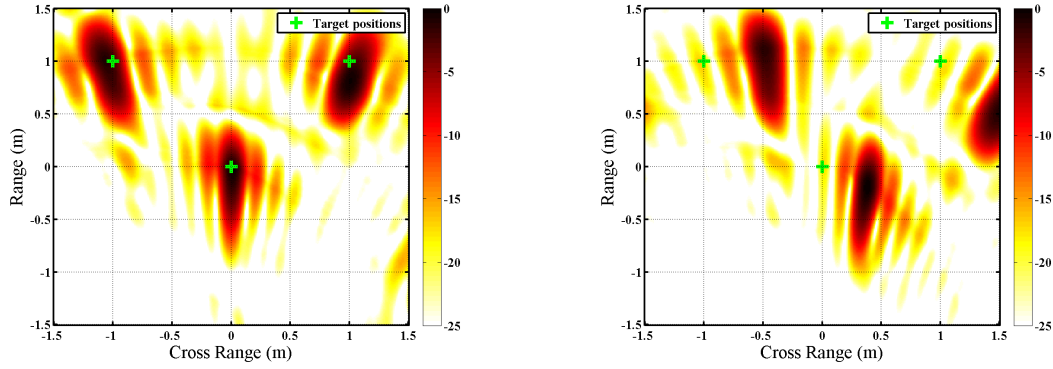
(b) Simulated ideal SAR image with autofocusing applied

Figure 24. Case II: Convex optimization applied with no error present.

3.4.2 Case II: Rotational error.

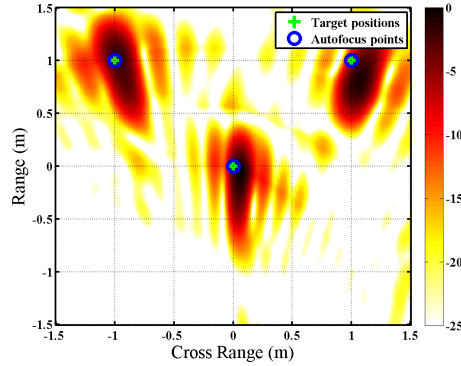
In this simulation (and in the actual laboratory), the receiver travels along a linear rail. In Case II, the receiver track is rotated by 10° in the xy-plane about the center point of the rail. The resultant SAR images produced for this case are shown in Figure 25. Note in Figure 25(b) that the targets still appear strongly but in the

wrong position. This is expected as the only error imputed to the receiver position was rotational, manifesting itself in the SAR image as a registration error.



(a) Simulated SAR image created using ideal receiver position vector.

(b) Simulated SAR image created with 10° skew error applied to receiver position vector.



(c) Simulated SAR image created from autofocused range profiles.

Figure 25. Case II: Convex optimization applied to skew error.

As evidenced by the results shown in Figure 25(c) the semidefinite relaxation autofocusing algorithm is able to compensate for the registration error.

Table 3. Case II Peak Target Reflections

Target	Ideal Value	Defocused Value	Autofocused Value
A	-0.04 dB	-17.83 dB	-2.09 dB
B	-1.91 dB	-17.48 dB	-2.01 dB
C	-2.92 dB	-20.31 dB	-6.36 dB

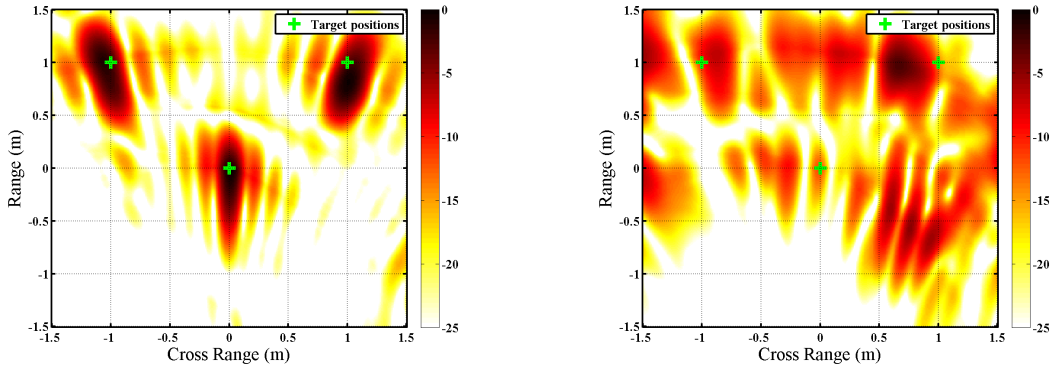
3.4.3 Case III: White noise error.

In case III, white noise positioning error is induced in each dimension by multiplying the ideal position by a pseudorandom uniform error term. The actual linear track used in the RAIL is very stable in the z-dimension, but has a slight wobble in the y-dimension. The x-dimension is the direction of travel and induces the greatest error into the position solution. As such, the random error distribution used in the simulation was $\mathcal{N}(0, 10 \text{ cm})$ in the x-direction, $\mathcal{N}(0, 5 \text{ cm})$ in the y-direction, and $\mathcal{N}(0, 1 \text{ cm})$ in the z-direction. Figure 26 shows the SAR images resulting from the ideal case, the defocused case, and the autofocused case.

Table 4 shows the peak target reflections for each target in the scene. The peak target values in the autofocused image are lower than the values in the ideal image. This reduction is attributed partly to the fast-time phase term ($\mathcal{D}(\tau)$) being removed in the autofocus derivation.

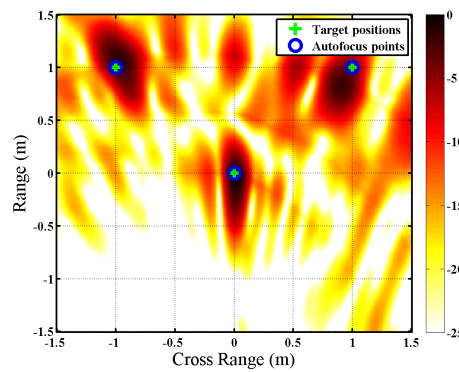
Table 4. Case III Peak Target Reflections

Target	Ideal Value	Defocused Value	Autofocused Value
A	-0.04 dB	-11.75 dB	-0.14 dB
B	-1.91 dB	-10.03 dB	-2.05 dB
C	-2.92 dB	-13.43 dB	-4.29 dB



(a) Simulated SAR image created using ideal receiver position vector.

(b) Simulated SAR image created with random error applied to receiver position vector.



(c) Simulated SAR image created from autofocus range profiles.

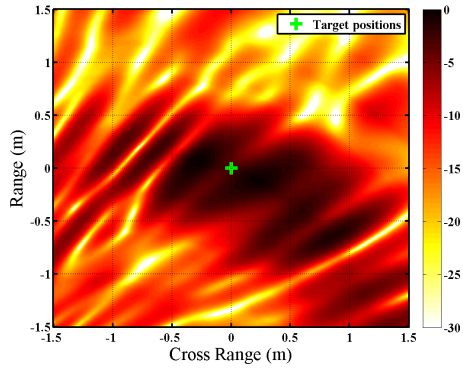
Figure 26. Case III: Convex optimization applied to white noise error.

3.5 Autofocus Applied to Experimental Results

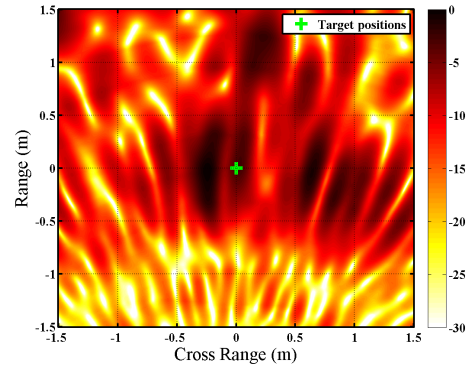
3.5.1 Example Results from Experimentation.

Section 3.4 showed the positive effects of an autofocusing algorithm on simulated SAR images, but the utility of the algorithm is fully displayed in its effect on experimentally collected data. Figure 27 shows an experimental SAR image before and after applying the autofocusing algorithm. In images from both antennas A. and B., a clear improvement in image interpretation is evidenced by a large return at scene center which corresponds to the single target's location.

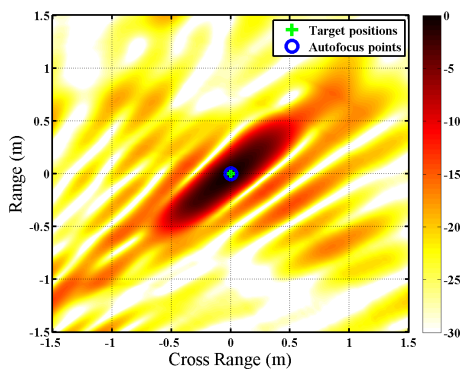
Algorithm effectiveness outside of the small laboratory environment is an even



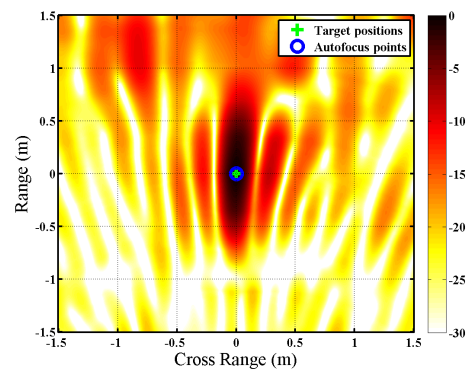
(a) Image created using raw data received by Antenna A.



(b) Image created using raw data received by Antenna B.



(c) Autofocused data from Antenna A.



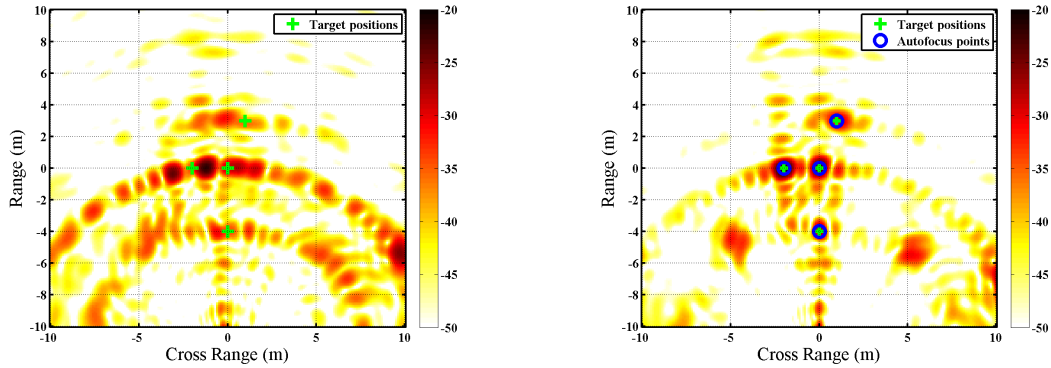
(d) Autofocused data from Antenna B.

Figure 27. Example SAR images showing the effects of autofocusing on experimental data. In all collections, a single target is located at scene center.

more significant question. While no large-scene data collections were conducted in the course of this research effort, previous researchers [1] used outdoor scenes extensively in passive bistatic collections. Figure 28 shows both a non-focused and autofocused image created using an outdoor scene 10 m across in both x and y dimensions. While this scene is small compared to many real-world SAR applications, it demonstrates the utility of the algorithm in capacities beyond indoor laboratory collections.

3.5.2 Robustness of Autofocusing Algorithm.

The autofocusing algorithm requires *a priori* knowledge of target locations. In most applications, target position will be estimated based on physical measurements

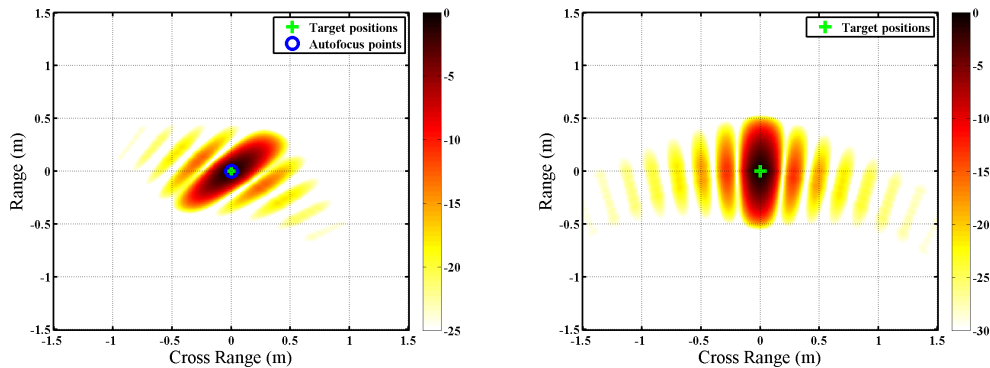


(a) Image created using raw data collected in [1]

(b) Autofocusing algorithm applied to imaging data collected in [1]

Figure 28. Autofocusing produces imaging enhancements in larger outdoor scenes in addition to smaller indoor laboratory scenes. Images are copied from [6].

or prior data collections. The sensitivity of the algorithm's effectiveness against target position error is qualitatively summarized in Figure 30. For comparison purposes, simulations of the ideal scenario with no imposed error are graphed in Figure 29.

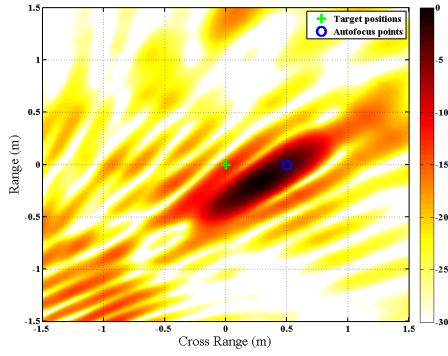


(a) Image from simulated data processed with no position error given the position of Antenna A.

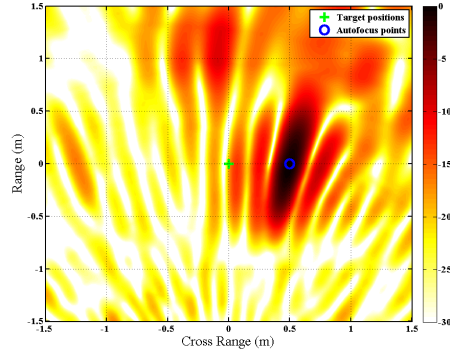
(b) Image from simulated data processed with no position error given the position of Antenna B.

Figure 29. Effects of position error in the x-direction on autofocusing performance.

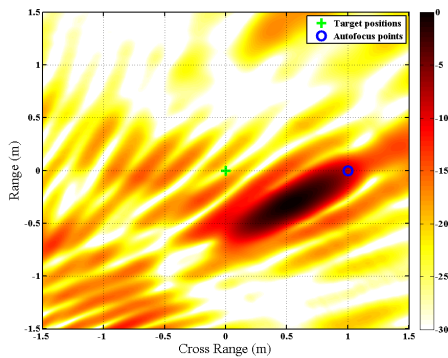
Each image in Figure 30 is processed by feeding the focusing algorithm an erroneous target location, as depicted in the figure captions. As the algorithm attempted focusing further away from scene center (the actual target location) image quality was degraded and more energy spilled into background. For comparison purposes,



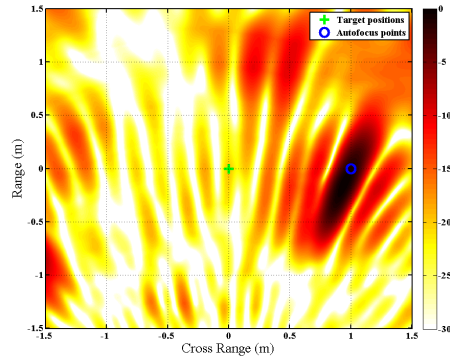
(a) Antenna A: Actual target at $(0,0)$, auto-



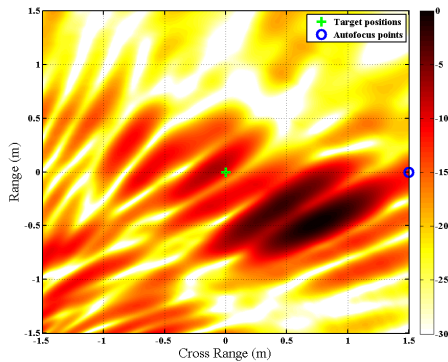
(b) Antenna B: Actual target at $(0,0)$, auto-



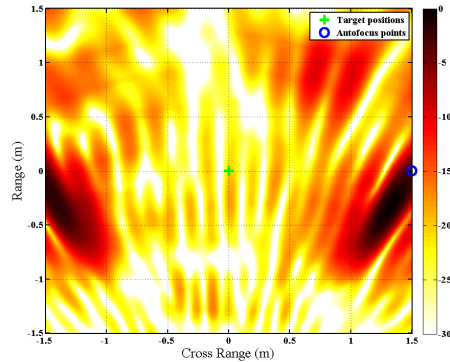
(c) Antenna A: Actual target at $(0,0)$, auto-



(d) Antenna B: Actual target at $(0,0)$, auto-



(e) Antenna A: Actual target at $(0,0)$, auto-

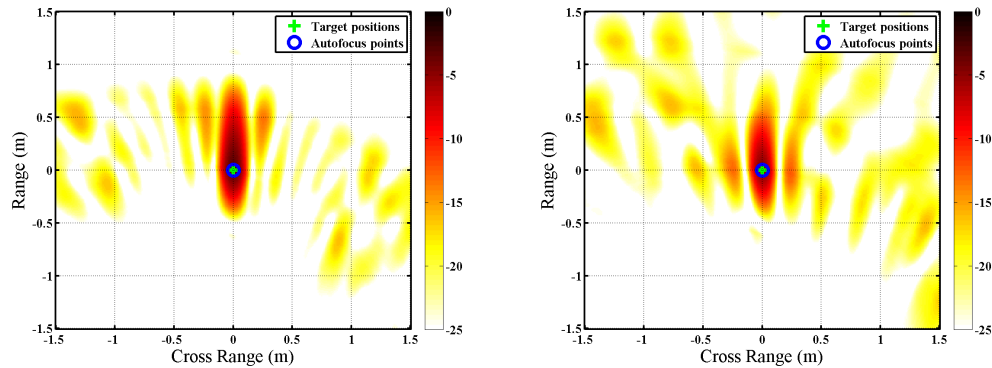


(f) Antenna B: Actual target at $(0,0)$, auto-

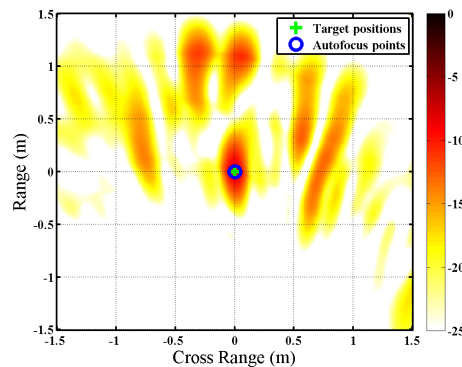
Figure 30. Effects of autofocusing at certain distance away from actual target location.

the correctly-focused image is Figure 29. When the target was placed near the scene's right edge (30(f)), imaging artifacts were aliased onto the left side of the image.

In Figure 31 the utility of the autofocusing algorithm is tested by feeding white noise error into the antenna position data. Such error could be caused by MME which has plagued this system since inception. Beginning with perfect position data in 29(b), the effects of white noise errors with standard deviations of 1 m, 2 m, and 3 m are exhibited in 31(a), 31(b), and 31(c) respectively.



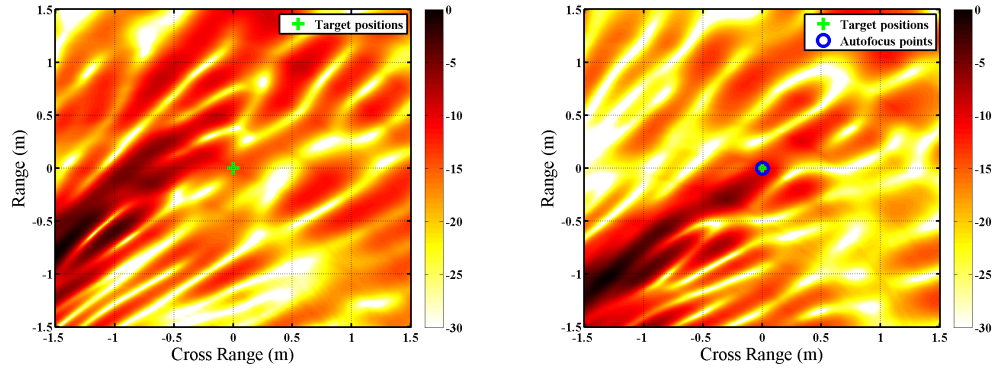
(a) Image from simulated phase history with white noise position error with standard deviation of 1 m. (b) Image from simulated phase history with white noise position error with standard deviation of 2 m.



(c) Image from simulated phase history with white noise position error with standard deviation of 3 m.

Figure 31. Effects of position error in the x-direction on autofocusing performance.

Another important characteristic of a focusing technique is that no false targets are created in an area of maximization. Figure 32(a) shows a laboratory background scene with no target present. Figure 32(b) represents an autofocused image of the background which was processed assuming there was a target present at scene center.



(a) Raw image of laboratory background with no targets present. (b) Image of laboratory background with no targets present focused at scene center.

Figure 32. Focusing at a point in the image where no target exists has negligible qualitative effects on image quality and no false targets are created at the point of maximization.

In this case, the focusing algorithm did not introduce a target reflection where there was not one before. All background collections were focused in this manner and no false targets were introduced into the scene, which is indicative of tremendous algorithm reliability.

3.6 Conclusion

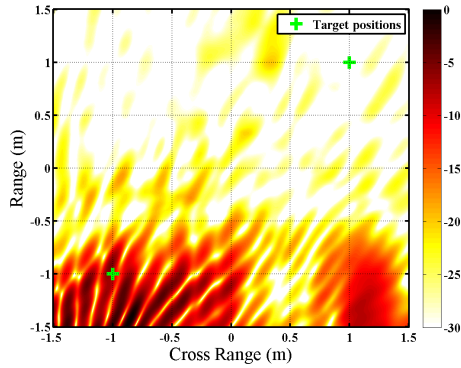
The analysis in this chapter expanded on work completed in [20, 21] and [6] by investigating the effects of specific phase errors in simulated phase history data and validating the effects of convex optimization on experimental bistatic SAR data. In Chapter IV, the autofocus algorithm will be used in further image analysis while showcasing the new utility of the SAR system.

IV. Final Imaging Results

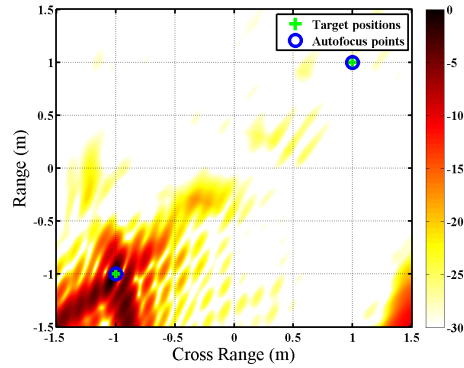
4.1 Dynamic range challenges

The scene in Figure 33(a) and 33(b) contains two targets located in the lower left and upper right portion of the scene. While both images accurately display an area of greater reflection in the lower left, it is difficult to determine the actual location of the targets in 33(a) because of the motion measurement errors present in the data. The large reflections of the target in the lower left is likely causing the reflections from the upper right target to be lost below the dynamic range of the plot scale. This is expected behavior as one target is over two meters closer to the antennas than the other and reflected power drops off at a rate of $R_T^2 R_R^2$ where R_T is the range from the transmitter to the target and R_R is the range from the receiver to the target.

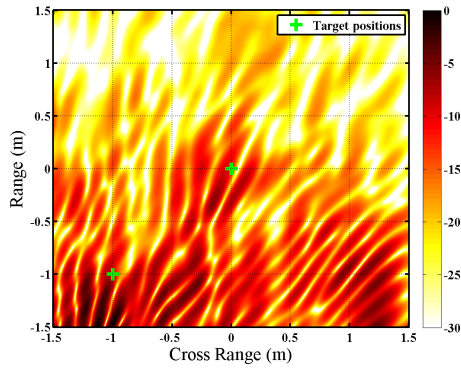
The scene in 33(c) and 33(d) show a similar configuration except that the furthest target is at scene center. The power reflected from this target does not completely fall below the dynamic range as evidenced by some returns in that area of the image.



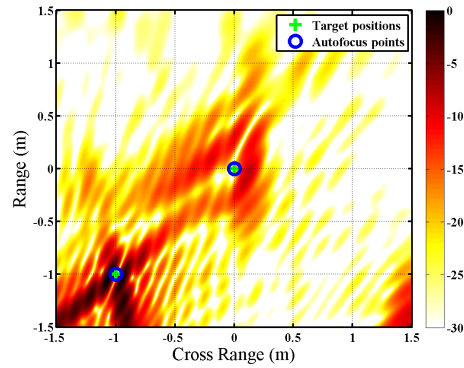
(a) Imaging data representing a multistatic summation from two receive paths.



(b) Imaging data from (a) with autofocus algorithm applied to the bistatic images before summation.



(c) Imaging data representing a multistatic summation from two receive paths.



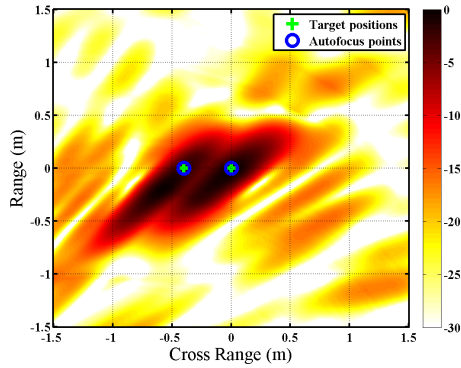
(d) Imaging data from (c) with autofocus algorithm applied to the bistatic images before summation.

Figure 33. Large target reflections in the foreground of the scene often cause targets in the background to drop below the dynamic range.

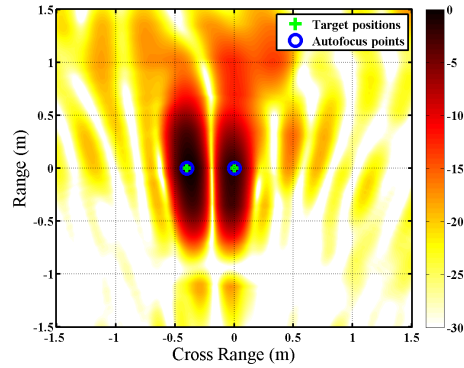
4.2 Resolution Analysis

Image resolution, as mentioned previously, is a significant parameter describing the performance of a SAR system. The ability to distinguish one scatterer in a scene from another is a characteristic defining the utility and possible mission for an imaging radar. This research employed targets 15 cm in diameter, and Figure 34 shows images created while incrementally moving these targets closer together.

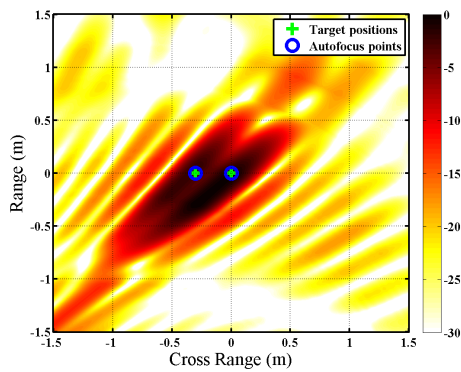
In the case of Antenna A, the targets are difficult to resolve at 0.3 m spacing and entirely impossible to resolve at 0.2 m. Antenna B images contain resolved targets



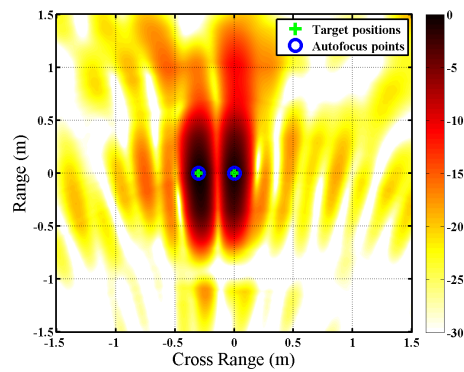
(a) Focused image from Antenna A. with targets spaced 0.4 m apart.



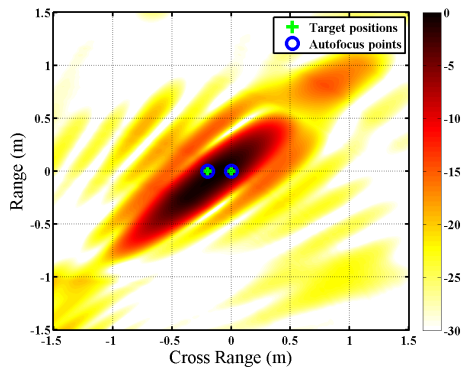
(b) Focused image from Antenna B. with targets spaced 0.4 m apart.



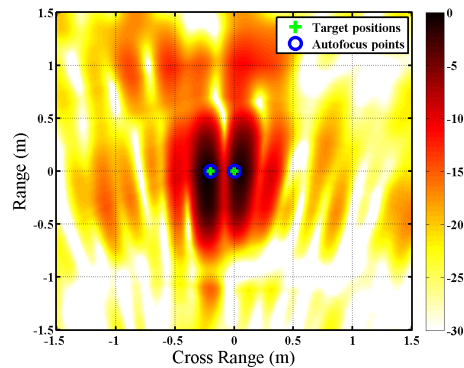
(c) Focused image from Antenna A. with targets spaced 0.3 m apart.



(d) Focused image from Antenna B. with targets spaced 0.3 m apart.



(e) Focused image from Antenna A. with targets spaced 0.2 m apart.



(f) Focused image from Antenna B. with targets spaced 0.2 m apart.

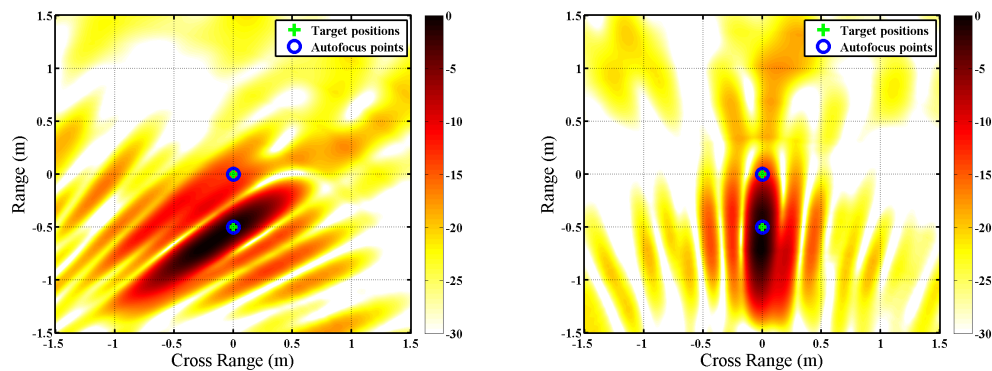
Figure 34. Resolution performance demonstrated by incrementally moving targets closer together in the x-direction.

all the way down to 0.2 m and the target diameter of 0.15 m is the only reason they were not moved closer. This behavior is expected as Antenna A observes the targets

from an oblique angle while Antenna B sees the maximum amount of space between them.

Still, resolution specifications are not close to the values recorded in Table 1 for antennas A and B as calculated in Chapter II. A simplifying assumption of the autofocusing algorithm limits position correction to the x-axis, which will serve to improve observed resolution in the x-direction while having little impact of resolution in the y-direction.

The configurations depicted in Figure 34 were repeated but using decreasing separation in the y-direction. Even at the widest separation, the targets were indistinguishable by Antenna B and questionably resolved by Antenna A as shown in Figure 35.



(a) Focused image from Antenna A. with targets spaced 0.4 m apart. (b) Focused image from Antenna B. with targets spaced 0.4 m apart.

Figure 35. Resolution performance demonstrated by incrementally scootching targets closer together in the y-direction.

Interestingly, in no configuration did multistatic processing render any improvement on qualitative resolution. This is predictive, as Antenna A struggled with resolving targets in nearly all scenarios, thus it had a negative impact on Antenna B in the multistatic realm.

4.3 Effects of Pulse Dropping on Image Quality

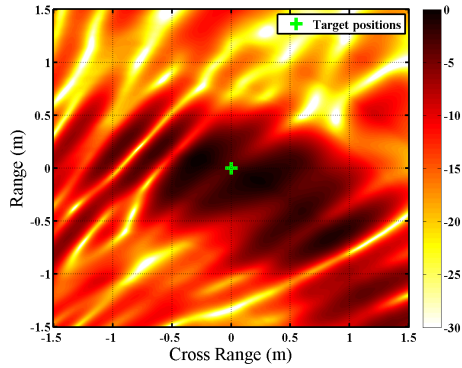
The author of [1] used components of the AFIT SAR system and hypothesized that the antenna acceleration and deceleration at the beginning and end of the linear track created position errors disproportionately large for the first and last pulses compared to the pulses received while the receiver was at a constant velocity. Dropping pulses from the collection will decrease the aperture extent which has the effect of enlarging the resolution and narrowing the scene size available before aliasing occurs.

Figure 36 shows original non-focused images in 36(a) and 36(b) followed by images created from the same data collections but with pulses trimmed from the ends. For both antennas, dropping pulses has the effect of gathering stronger returns around the target location (scene center). Dropping eight pulses from a collection also has the effect of aliasing targets into the scene on the left and right of scene center as shown in 36(e) and 36(f).

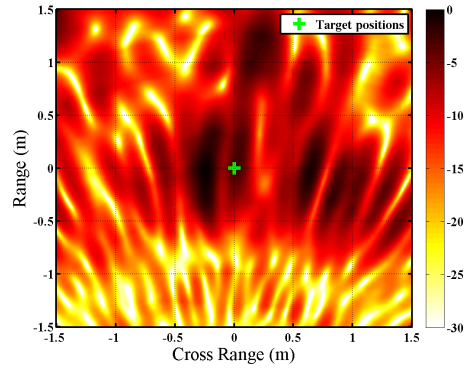
The same effect is not observed when images are focused. As shown in Figure 37, dropping four pulses causes additional clutter in the scene background while dropping eight causes strong target aliasing into the scene edges. The fact that focused images are degraded by pulse dropping makes intuitive sense as the purpose of focusing is to correct for the position errors of the fringe pulses. Since these errors are mostly corrected in Figures 37(a) and 37(b), dropping additional pulses has the negative effect of excluding good data from post processing.

4.4 Extended Aperture Processing Comparison

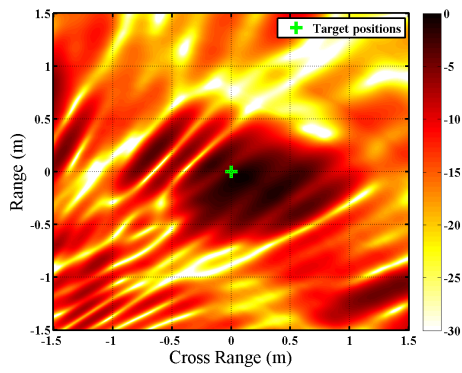
Bistatic images from multiple antennas may be integrated into a multistatic image via coherently summing all images or concatenating pulses and processing as a single collection as discussed in 2.5.4. Figure 38 compares results gleaned from these two approaches. Figures 38(a) and 38(b) are bistatic collections and Figure 38(c) shows



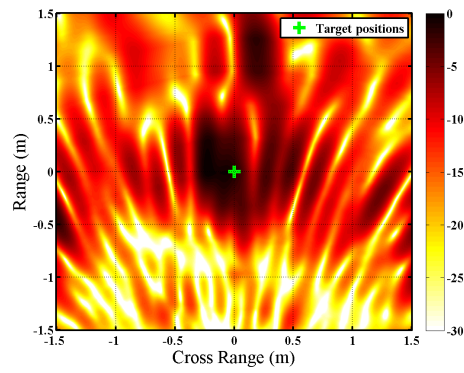
(a) Raw image processed from 16 pulses from Antenna A.



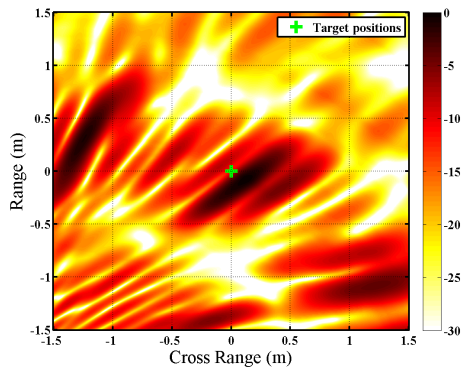
(b) Raw image processed from 16 pulses from Antenna A.



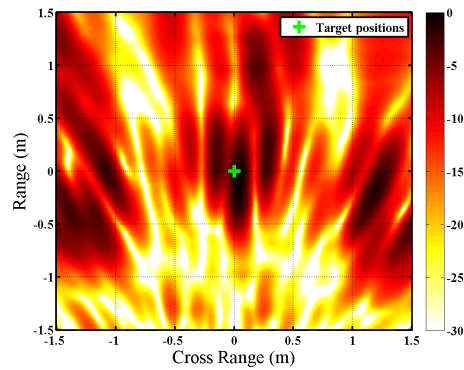
(c) Raw image with 4 pulses dropped (2 from each end) from Antenna A.



(d) Raw image with 4 pulses dropped (2 from each end) from Antenna B.



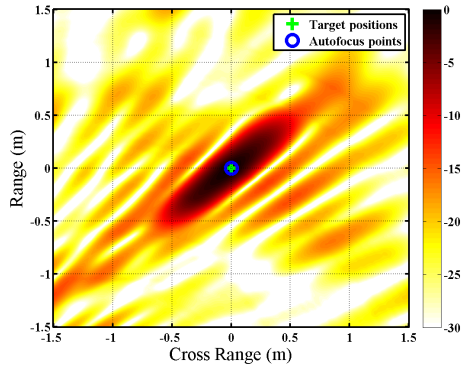
(e) Raw image with 8 pulses dropped (4 from each end) from Antenna A.



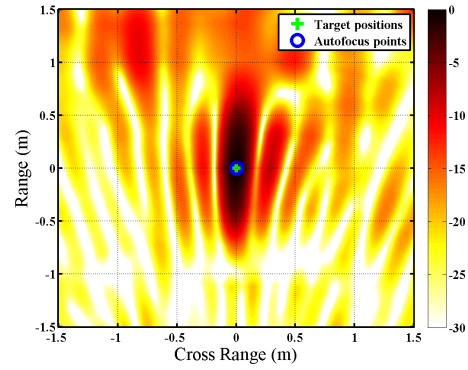
(f) Raw image with 8 pulses dropped (4 from each end) from Antenna B.

Figure 36. The effects of pulse dropping on SAR image quality with a single target located at scene center

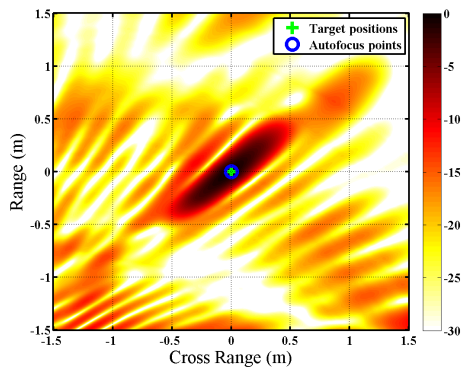
the results from coherent summation while Figure 38(d) represents extended aperture processing. Both demonstrate a qualitative improvement in target detection versus



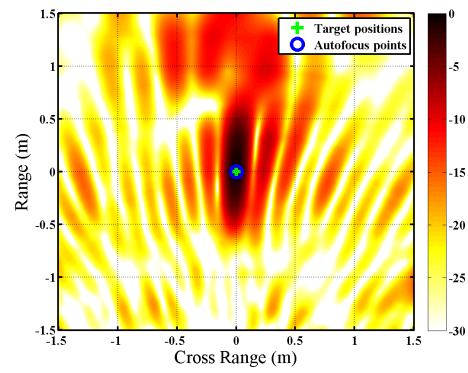
(a) Raw image processed from 16 pulses from Antenna A.



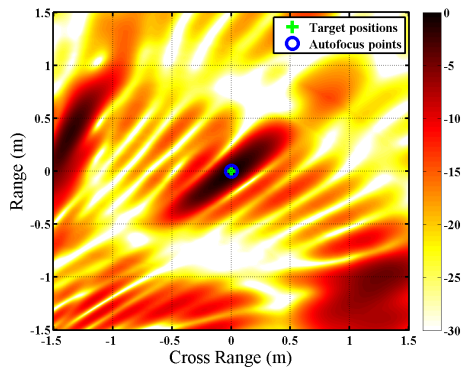
(b) Raw image processed from 16 pulses from Antenna B.



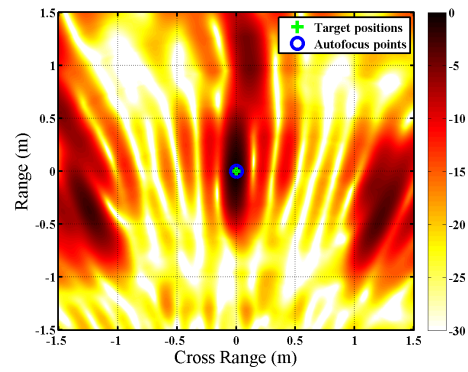
(c) Raw image with 4 pulses dropped (2 from each end) from Antenna A.



(d) Raw image with 4 pulses dropped (2 from each end) from Antenna B.



(e) Raw image with 8 pulses dropped (4 from each end) from Antenna A.

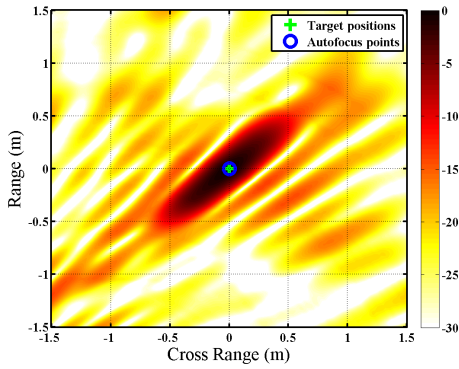


(f) Raw image with 8 pulses dropped (4 from each end) from Antenna B.

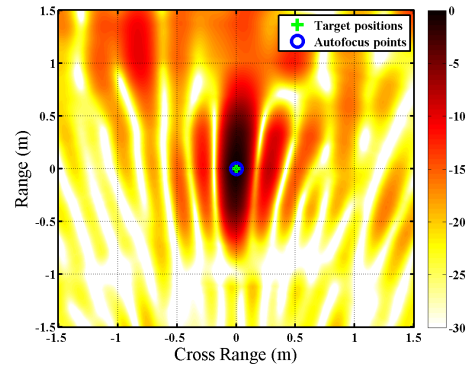
Figure 37. The effects of pulse dropping on SAR image quality with a single target located at scene center

bistatic images, but Figure 38(d) has a single, smaller target lobe and overall lower image clutter. The split lobes in Figure 38(d) may cause confusion given that only

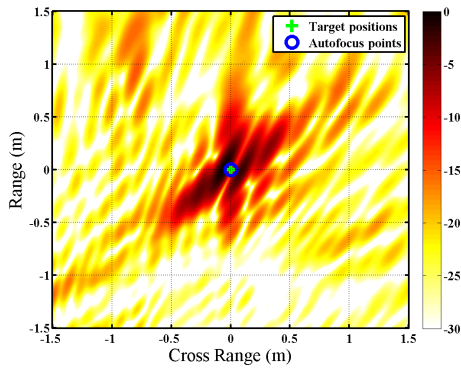
one target is present (compare to two-target image in Figure 39(b)).



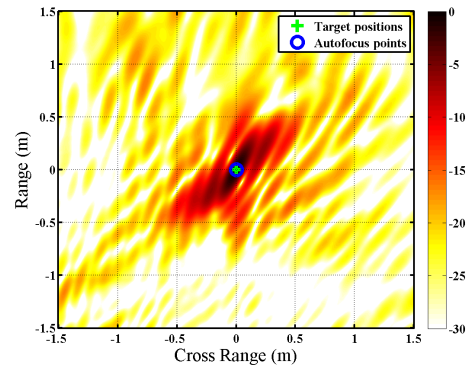
(a) Autofocused image of target at scene center from Antenna A.



(b) Autofocused image of target at scene center from Antenna B.



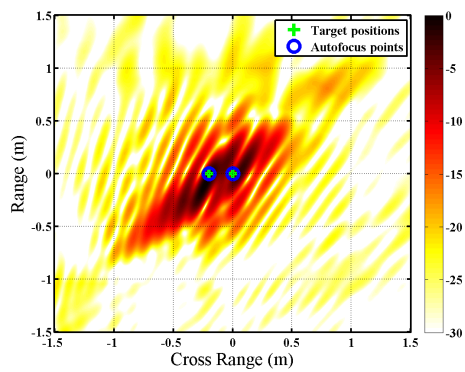
(c) Multistatic image created using summation



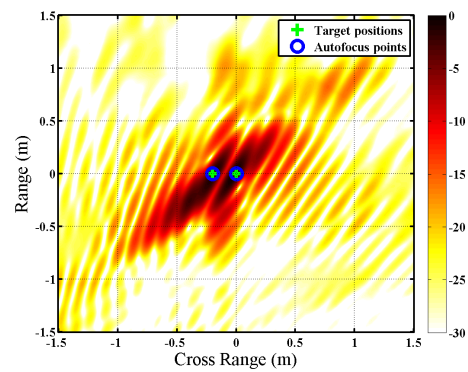
(d) Image created using extended aperture processing

Figure 38. In this case involving a target at scene center, extended aperture processing yields a single, smaller target lobe versus the split lobe resulting from image summation.

Extended aperture processing also yields some qualitative improvement in resolution. Figure 39 compares the two processing types on a scene with closely spaced targets. The target lobes in Figure 39(b) are more clearly separated compared to those in Figure 39(a).



(a) Multistatic image created using summation.



(b) Image created using extended aperture processing.

Figure 39. Extended aperture processing appears to have some effect on qualitative ability to distinguish closely spaced targets, as the target lobes in (b) are clearly divided.

V. Conclusions and Future Work

This thesis has only scratched the surface of the potential the AFIT SAR system has as a tool for experimentation and analysis. This chapter summarizes findings from this research effort and suggests areas for improvement and future exploration.

5.1 Summary

This thesis successfully improved the AFIT RAIL SAR system by expanding its data collection methods from bistatic to multistatic. Prior “guess and test” calibration factors were replaced with an automated calibration routine. Two multistatic synthesis techniques were applied to SAR images with observed performance improvements.

An autofocusing algorithm which had never been applied to experimental data was evaluated against various error magnitudes and finally applied to experimental images from the radar resulting in significant improvements to image quality and target recognition. General observations were made regarding image limitations and challenges associated with data collection and image processing techniques.

5.2 Future work

A laboratory SAR system is a blank slate for further investigation and analysis in the areas of hardware configuration, target characteristics, collection methods, and signal processing approaches. Suggested areas for further exploration include:

- Identify, investigate, and mitigate other errors present in the radar system to improve image quality.
- Employ transmit signal sensing, identification, and estimation to transform the radar into a true passive system requiring no cooperation with the transmitter.

- Explore the benefits of signal mixing to reduce the required sampling rate and data size.
- Explore more scene geometries and target types, including moving targets to evaluate the effects of Doppler shift error on image quality.
- Add a second transmit antenna to the AWG or employ an entirely separate transmit antenna to expand multistatic analysis capabilities.
- Rewrite the “move-stop-move” portion of the radar controller code to enable quicker data collections. This methodology has proven to be superior to the techniques involving constant receiver motion but was abandoned in this research effort because of collection time.
- Rewrite post processing code to enable 3D image production.
- Expand the signal model to include noise and Doppler effects.
- Examine the effect and limitations of ignoring the fast-time phase term in the autofocus problem formulation.

2D two-dimensional

3D three-dimensional

AFIT Air Force Institute of Technology

AFRL Air Force Research Laboratory

AWG arbitrary waveform generator

BPA backprojection algorithm

CBP convolution backprojection

DAB Digital Audio Broadcasting

GUI graphical user interface

IEEE Institute of Electrical and Electronics Engineers

MME motion measurement error

OFDM orthogonal frequency division multiplexing

PRI pulse repetition interval

PRF pulse repetition frequency

RAIL Radar Instrumentation Laboratory

RCS radar cross section

RF radio frequency

SAR synthetic aperture radar

WiMAX Worldwide Interoperability for Microwave Access

Bibliography

1. D. A. Schmidt, “Hardware development and error characterisation for the AFIT RAIL SAR SYSTEM,” Master’s thesis, Air Force Institute of Technology, March 2016.
2. J. Gutierrez del Arroyo, “Passive synthetic aperture radar imaging using commercial OFDM communication networks,” Ph.D. dissertation, Air Force Institute of Technology, Sep. 2012.
3. A. S. Evers, “Evaluation and application of LTE, DVB, and DAB signals of opportunity for passive bistatic SAR imaging,” Master’s thesis, Wright State University, April 2014.
4. C. Jakowatz, D. Wahl, P. Eichel, D. Ghiglia, and P. Thompson, *Spotlight-Mode Synthetic Aperture Radar: A Signal Processing Approach*. Norwell, MA: Kluwer Academic Publishers, 1996.
5. G. W. Stimson, *Airborne Radar*. Mendham, NJ: SciTech Publishing, Inc., 1998.
6. A. S. Evers, N. Zimmerman, and J. A. Jackson, “Semidefinite relaxation autofocus for bistatic backprojection SAR,” in *IEEE Radar Conference*, May 2017, pp. 1–6.
7. A. S. Evers and J. A. Jackson, “Experimental passive SAR imaging exploiting LTE, DVB, and DAB signals,” in *IEEE Radar Conference*, May 2014, pp. 0680–0685.
8. —, “Analysis of an LTE waveform for radar applications,” in *IEEE Radar Conference*, May 2014, pp. 0200–0205.
9. —, “Cross-ambiguity characterization of communication waveform features for passive radar,” *IEEE Transactions on Aerospace and Electronic Systems*, vol. 51, no. 4, pp. 3440 – 3455, October 2015.
10. *TDS6000B & TDS6000C Series Digital Storage Oscilloscopes Quick Start User Manual*, Tektronix, Jan 2006.
11. “AirMax sector antenna datasheet,” Ubiquiti Networks Inc., 2013. [Online]. Available: https://dl.ubnt.com/datasheets/airmaxsector/airMAX_Sector_Antennas_DS.pdf
12. E. F. Knott, J. F. Shaeffer, and M. T. Tuley, *Radar Cross Section*. Norwood, MA: Artech House, 1993.
13. C. Oliver and S. Quegan, *Understanding Synthetic Aperture Radar Images*. Raleigh, NC: SciTech Publishing, Inc., 2004.

14. S. Taylor, G. Antonello, and S. Rogers, "OFDM frame structure," IEEE 802.16 Broadband Wireless Access Working Group, Tech. Rep., January 2011. [Online]. Available: http://www.ieee802.org/16/tga/contrib/C80216a-02_16.pdf
15. J. Munson, D.C., J. O'Brien, and W. Jenkins, "A tomographic formulation of spotlight-mode synthetic aperture radar," *Proceedings of the IEEE*, vol. 71, no. 8, pp. 917–925, Aug 1983.
16. W. Carara, R. Goodman, and R. Majewski, *Spotlight Synthetic Aperture Radar Signal Processing Algorithms*. Artech House, Inc, 1995.
17. N. Willis and H. Griffiths, Eds., *Advances in Bistatic Radar*. Raleigh, NC: SciTech Publishing, Inc., 2007.
18. A. S. Evers, "SAR Imaging Autofocus Using Convex Optimization," Technical Report, EENG 899. Advanced Convex optimization with Application to Radar Signal and Image Processing, Air Force Institute of Technology, Dr. Julie Jackson,.
19. K. Liu, A. Wiesel, and D. Munson, "Synthetic aperture radar autofocus via semidefinite relaxation," *IEEE Transactions on Signal Processing*, vol. 22, no. 6, pp. 2317–2326, June 2013.
20. K. Liu, A. Wiesel, and D. C. Munson Jr., "Synthetic aperture radar autofocus via semidefinite relaxation," in *IEEE Transactions on Image Processing*, vol. 22, June 2013, pp. 2317–2326.
21. —, "Synthetic aperture radar autofocus via semidefinite relaxation," in *IEEE International Conference on Acoustics Speech and Signal Processing (ICASSP)*, March 2010, pp. 1342–1345.

REPORT DOCUMENTATION PAGE

Form Approved
OMB No. 0704-0188

The public reporting burden for this collection of information is estimated to average 1 hour per response, including the time for reviewing instructions, searching existing data sources, gathering and maintaining the data needed, and completing and reviewing the collection of information. Send comments regarding this burden estimate or any other aspect of this collection of information, including suggestions for reducing this burden to Department of Defense, Washington Headquarters Services, Directorate for Information Operations and Reports (0704-0188), 1215 Jefferson Davis Highway, Suite 1204, Arlington, VA 22202-4302. Respondents should be aware that notwithstanding any other provision of law, no person shall be subject to any penalty for failing to comply with a collection of information if it does not display a currently valid OMB control number. **PLEASE DO NOT RETURN YOUR FORM TO THE ABOVE ADDRESS.**

1. REPORT DATE (DD-MM-YYYY) 23-03-2017		2. REPORT TYPE Master's Thesis		3. DATES COVERED (From — To) Sept 2015 — Mar 2017		
4. TITLE AND SUBTITLE The Effects of Multistatic Processing and Autofocusing on an Experimental Passive Synthetic Aperture Radar Imaging System				5a. CONTRACT NUMBER		
				5b. GRANT NUMBER		
				5c. PROGRAM ELEMENT NUMBER		
				5d. PROJECT NUMBER		
				5e. TASK NUMBER		
6. AUTHOR(S) Zimmerman, Nicolas H., Capt, USAF				5f. WORK UNIT NUMBER		
7. PERFORMING ORGANIZATION NAME(S) AND ADDRESS(ES) Air Force Institute of Technology Graduate School of Engineering and Management (AFIT/EN) 2950 Hobson Way WPAFB OH 45433-7765			8. PERFORMING ORGANIZATION REPORT NUMBER AFIT-ENG-MS-17-M-085			
9. SPONSORING / MONITORING AGENCY NAME(S) AND ADDRESS(ES) Air Force Research Laboratory, Sensors Directorate 2241 Avionics Circle, Bldg 600 WPAFB OH 45433-7318 Dr. Muralidhar Rangaswamy Email: muralidhar.rangaswamy@us.af.mil, Phone: 937-713-8567			10. SPONSOR/MONITOR'S ACRONYM(S) AFRL/RV			
			11. SPONSOR/MONITOR'S REPORT NUMBER(S)			
12. DISTRIBUTION / AVAILABILITY STATEMENT DISTRIBUTION STATEMENT A: APPROVED FOR PUBLIC RELEASE; DISTRIBUTION UNLIMITED.						
13. SUPPLEMENTARY NOTES This material is declared a work of the U.S. Government and is not subject to copyright protection in the United States.						
14. ABSTRACT The Air Force Institute of Technology (AFIT) Radar Instrumentation Lab (RAIL) Synthetic Aperture Radar (SAR) experimental system is capable of bistatic passive SAR collections. This research assesses current system limitations and expands the hardware and software to facilitate multi-static imaging in experimental and simulated configurations. An autofocusing algorithm is applied to phase history data to mitigate position error and improve image quality in both bistatic and multi-static cases. Final experimental results show significant improvement to imaging products attributed to these signal processing techniques.						
15. SUBJECT TERMS synthetic aperture radar (SAR), passive radar, multistatic radar, autofocus, error characterization, motion measurement errors (MME)						
16. SECURITY CLASSIFICATION OF:			17. LIMITATION OF ABSTRACT UU	18. NUMBER OF PAGES 78	19a. NAME OF RESPONSIBLE PERSON Dr Julie Jackson,(ENG)	
a. REPORT U	b. ABSTRACT U	c. THIS PAGE U			19b. TELEPHONE NUMBER (include area code) (937) 255-3636 x4678; julie.jackson@afit.edu	